https://doi.org/10.1016/j.compgeo.2021.104383

Investigating the effect of particle angularity on suffusion of gap-graded soil using coupled CFD-DEM

Author 1

Jian-Gu QIAN, Professor

Key Laboratory of Geotechnical and Underground Engineering of Ministry of Education, China; Department of Geotechnical Engineering, College of Civil Engineering, Tongji University, China.

Author 2

Chuang ZHOU, PhD candidate

Key Laboratory of Geotechnical and Underground Engineering of Ministry of Education, China; Department of Geotechnical Engineering, College of Civil Engineering, Tongji University, China.

Author 3

Zhen-Yu YIN, Associate Professor

Department of Civil and Environmental Engineering, The Hong Kong Polytechnic University, Hong Kong, China.

Author 4

Wei-Yi LI, PhD candidate

Key Laboratory of Geotechnical and Underground Engineering of Ministry of Education, China; Department of Geotechnical Engineering, College of Civil Engineering, Tongji University, China.

*Corresponding author

Dr. Zhen-Yu YIN, Tel: +852 3400 8470; Fax: +852 2334 6389;
Email: zhenyu.yin@polyu.edu.hk, zhenyu.yin@gmail.com

Abstract:

Influence of particle angularity on the suffusion in gap-graded granular soils remains unclear up to now. In this study, systematical numerical simulations that consider the particle shape as quasi-spherical polyhedra in different angularity are performed with the coupled discrete element method (DEM) and the computational fluid dynamics (CFD) approach. The suffusion of six gap-graded soil samples with 25% fines content is examined by imposing an upward seepage flow. Conventional triaxial tests are also conducted on the pre-eroded and post-eroded specimens to study the coupling influence of angularity and suffusion on the mechanical characteristics of granular soils. Fines loss, vertical displacement, soil strength, volume flow rate, microstructural analyses of force networks, the cumulative percentage of contact force, and the anisotropy of contact are investigated. Results turn out that the angularity intensifies the internal erosion resistance as the fines loss decreases significantly with the increasing angularity. The soil peak strength and friction angle are approximately linearly correlated with angularity. Erosion-induced particle redistribution reduces the degree of anisotropy of contact normal and contact normal force. This study may improve our understanding of the effect of particle angularity on suffusion with both microscopic and macroscopic evidence.

Keywords: CFD-DEM; suffusion; angularity; polyhedral particles; gap-graded soils

1 Introduction

For gap-graded granular soils, fine particles may migrate through the pores connected by coarse fractions when they are subjected to external hydraulic force, which can be defined as suffusion erosion (Liu et al., 2020a). The fines loss may lead to a progressive degradation in soil mechanical properties, raising the risk of failure for geotechnical structures (e.g., tunnels, slopes, dams) (Chang and Yin, 2011; Fell et al., 2003; Foster et al., 2000; Yin et al., 2016). The hazard of suffusion has motivated many studies on revealing its mechanism. According to the available literature, the initiation and progression of suffusion are governed by many factors, including grain size distribution (GSD) (Benamar and Bennabi, 2015; Kim et al., 2019; Wan and Fell, 2008), confining pressure (Liang et al., 2019; Shire et al., 2014), initial fines content (Ke and Takahashi, 2012; Yang et al., 2020a, 2019a) as well as hydraulic gradient (Fonseca et al., 2012; Indraratna et al., 2011). Recently, many studies pointed out that suffusion is also closely associated with particle shape (e.g., the angularity and roundness of particle) (Hu et al., 2020; Xiong et al., 2020), which simultaneously governs the interparticle force and hydraulic force. Unfortunately, there are still no detailed studies on the influence of particle angularity on suffusion up to now.

Previous theoretical analysis (Horikoshi and Takahashi, 2015; Yang et al., 2020b, 2020a, 2019b) and physical experiments (Israr and Irfan, 2020; Ni et al., 2004; Pitman et al., 1994; Reddi et al., 2000) have laid a foundation to gain a first insight into suffusion. Nevertheless, fine particles within the soils will be eroded during the suffusion so that the continuum mechanics is no longer applicable. Currently, numerous numerical simulations of such problems have been carried out by the coupled computational fluid dynamics (CFD) and the discrete element method (DEM) since Zhao and Shan (2013) firstly introduced this approach into mining and geotechnical engineering. In this method, the interparticle forces and fluid-particle forces can be analyzed separately. The migration trajectory of each particle and the redistribution of force chains due to particle reorganization can also be visualized. Compared to the macroscopic level studies of experiments, the coupled DEM-CFD has a natural advantage in understanding the fundamental mechanism from a microscopic viewpoint (Yang et al., 2017). For example, Xiong et al. (2020) investigated the effect of flow direction in suffusion based on the CFD-DEM approach and concluded that the greater the angle between gravity and flow, the harder suffusion occurs. Liu et al. (2020a) examined the effect of fines content and confining pressure, shedding micromechanical insights into the macroscopic phenomenon of suffusion. Hu et al.

(2020) studied the preparation of specimens in DEM and pointed out that different particle generation methods can lead to qualitatively different conclusions in suffusion. However, it should be noted that the shapes were assumed to be the perfect 3D spheres in their studies, whereas naturally formed sandy particles are not a regular sphere due to the physicochemical effects in their formation. In other words, the effect of particle shape in suffusion has not been considered.

Various shapes have been conducted to investigate the effect of particle shape in the DEM simulations. Up to now, the commonly used representations of DEM irregular shape are summarized as follows (Zhong et al., 2016): (1) Polygons and polyhedrons, for which particles are defined as the collection of corners, edges, and faces. The representation has developed into the most popular approach to model real particles in soils and rock issues, as it can simulate the angularity and roughness of the particle surface very well (Kohring et al., 1995; Wachs et al., 2012). (2) Continuous function representations, by which regular nonspherical particles can be simulated. For a specific particle, continuous function representations (CFR) implicitly describe the shape using a series of continuous functions in the Cartesian coordinate system (Cleary, 2008; Mustoe and Miyata, 2001). It believes that 80% of particles' shapes with symmetry can be realized by the continuous function of superquadrics or higher-dimensional hyper-quadrics (Williams and Pentland, 1989), whereas CFR has difficulty modeling arbitrary irregular particles. (3) Virtual space method, using which the arbitrary space shape is digitized by a coherent collection of pixels and voxels based on digitization (Hogue, 1998). These discrete digital cells form a virtual space, representing the real space occupied by the objected particles. The information used to reproduce different shapes is obtained by scanning real particles through 3D optical and X-ray scanners (Lu et al., 2012; Williams and O’connor, 1995). (4) Combined geometric element method (also known as clump), which simulates arbitrary particles by a group of essential elements, such as planar discs and spheres (Dong et al., 2015; Guo et al., 2013). Combining the essential elements to approximate the real particle shape, theoretically, the more essential elements used, the better the approximation effect (Guo et al., 2012). Unfortunately, an excessive number of essential elements will seriously increase the computational burden, and the clumps consisting of spheres cannot reflect the angularity of real particles.

In addition to the different particle shape representations, the particle shape's accurate quantification is also of great essence. There are three indexes (e.g., form, roughness, sphericity) to characterize the shape dissimilarity from different scales (Zhao and Wang, 2016). At a large scale, the form indicates the principle size and entire shape; at an intermediate scale, the roundness indicates the changes in corners; at a small scale, the roughness indicates the surface texture. When the soils are subjected to hydraulic action, as in the case of suffusion erosion studied in this paper, the interparticle forces are closely related to the roundness due to the resistance torque between the particles increases as the shape of the particles changes from 'well-rounded' to 'angular' (Zhu et al., 2020). Numerous studies have tried to explore the influence of angularity. For example, Zhao et al.(Zhao et al., 2015) firstly proposed a quasi-spherical polyhedron to reflect the change of particle angularity and applied them in the simulations of direct shear tests, indicating that the soil shear resistance is enhanced by particle angularity. Zhao arbitrated the phenomenon to the interlocking force between the nonspherical particles, which is confirmed by Yin et al. (2020). Nie et al. (Nie et al., 2020) explored the change of angularity caused by erosion in the triaxial tests, concluding that the peak shear strength and critical states decrease with decreasing angularity. Xiong et al. (Xiong et al., 2021) studied the effect of aspect ratio on suffusion with the CFD-DEM approach. The coarse particles adopted in their paper were nonspherical particles, whereas the fines were still assumed to be standard spheres. In addition, the effect of particle shape and suffusion on mechanical properties was not examined.

The main objective of this study is to investigate the effect of angularity on the suffusion of gap-graded sand samples. The particle shapes adopted are quasi-spherical polyhedra with different vertexes in a wide range of angularity. Based on the coupled DEM-CFD method, the simulated macro responses (including void ratio, fines loss, vertical displacement) and micro responses (including force transfer and particles spatial rearrangement) are presented, showing a significant role played by angularity. Triaxial tests are also performed on both pre-eroded and post-eroded samples.

2 Methodology of coupled CFD-DEM

The simulations in this study are enabled by combining the computational fluid dynamics (CFD) and the discrete element method (DEM). The coupling method is proposed by Kloss et al. (2012), and its reliability and accuracy have been confirmed by previous researches (Hu et al., 2020; Liu et al., 2020a; Nguyen and Indraratna, 2020; Xiong et al., 2020). The particle shape employed in this paper and governing equations of the coupling method will be introduced below.

2.1 Particle shape

The particle shape adopted in this paper is quasi-spherical polyhedral (Zhao et al., 2015), which has different vertexes neglecting the non-convexity and eccentricity effect, thereby only angularity being considered (as shown in Fig.1). A polyhedron with *N* bounding planes can be defined using a set of inequalities:

$$P = \left\{ (x, y, z) \middle| \; a_i x + b_i y + c_i z \le d_i, \quad i = 1, \ldots, N \right\} \tag{1}$$

where (a_i, b_i, c_i) is the normal vector of the plane i , d_i is the distance of the plane to the coordination origin.

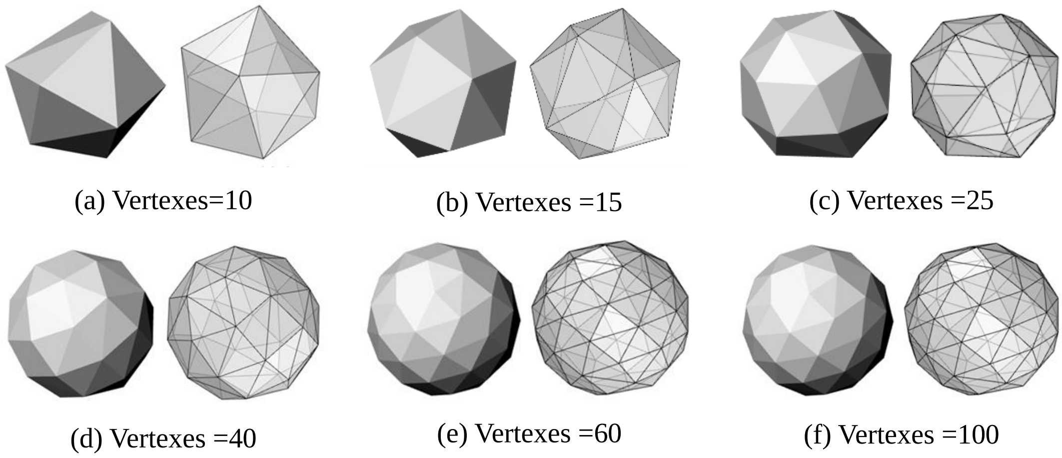

Fig. 1. Quasi-spherical polyhedral particle shapes with different vertexes.

The DEM domain calculates the forces acted on particles based on the contact area (i.e., overlap), which means that only if there is a conjecture overlap between two particles will there be a mutual contact force between them. For spheres, whose contact can be detected by comparing the distance between their centers and the sum of their radius. Nevertheless, for nonsphere particles, the overlap between two quasi-spherical polyhedral particles is the intersection for two sets of inequalities (Eq. (1)). This paper introduces a common plane (Cundall, 1988) to figure whether two polyhedral particles are in contact. If a plane defined as $S = \left\{ (x, y, z) \middle| \; a_s x + b_s y + c_s z = d_s \right\}$ can divide all the vertices of particle A on one side and all the vertices of particle B on the other, then it means the two particles don't contact. If such a plane does not exist, the particles are touching (as shown in Fig.2, two particles have a contact line and overlap volume).

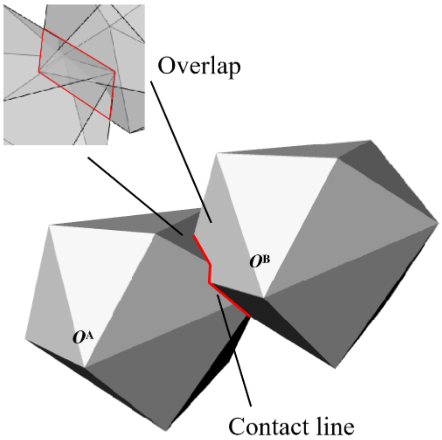

Fig. 2 Three-dimensional illustration of the interaction between two particles.

The normal orientation of contact for spheres is defined as the vector connecting two spherical centers, whereas, for the polyhedral particles, the vector is determined utilizing the least-squares fitting method (Eliáš, 2014). Based on the contact line (see the red line in Fig.2), which can be obtained by solving the set of bounding faces inequalities, a fitting plane can be determined (as shown in Fig.3). The vector perpendicular to the fitting plane through the mass center of overlap is defined as the normal contact direction of polyhedral particles.

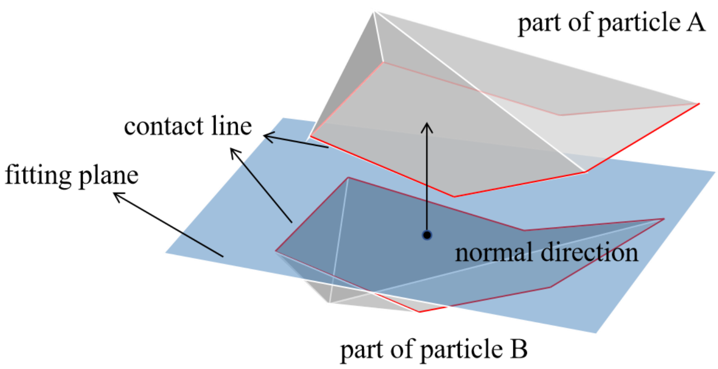

Fig. 3. Contact and fitting plane between polyhedral particles.

2.2.1 Governing equations of the DEM

The motivation of massive dispersed particles is governed by Newton's law. Given a specific time t and particle i , the translation and rotational motion of the particle can be calculated by:

$$m_i \frac{dv_i}{dt} = \sum_{j=1}^{j=n} F_{ij}^n + \sum_{j=1}^{j=n} F_{ij}^t + F_i^f + F_i^g \tag{2}$$

$$I_i \frac{d\omega_i}{dt} = \sum_{j=1}^{j=n} M_{ij} \tag{3}$$

where the subscript i denotes the particle number; the m_i is the particle's mass; v_i and ω_i represents the translational and angular velocity, respectively; F_{ij}^{n} and F_{ij}^{t} are the normal and tangential contact force acting on the particle i by particle or wall at the contact point j , and n means the total number of contacts the particle i engaged; I_i denotes the moment of inertia and M_{ij} is the torque acting on particle i by particle j; F_i^{f} is the particle-fluid interaction force acting on particle i, while F_i^{g} is imposed by gravity. In this paper, the Herts-Mindlin contact force model, which is generally adopted to characterize certain critical features of granular soils (Hu et al., 2020, 2019; Liu et al., 2020a; Xiong et al., 2020; Yang et al., 2020b), is employed to calculate the interparticle forces. Both the elastic and the damping components are non-linear functions of the contact overlap.

2.2.2 Governing equations of the CFD

In this paper, the CFD domain is partitioned into a finite number of volume cells, where the pressure and velocity are averaged. By iteratively solving the averaged Navier-Stokes (N-S) equation, the velocity and pressure of any cell at a certain time can be obtained. Accounting for the presence of particles in the fluid, the locally averaged N-S equation is written as:

$$\frac{\partial \alpha_f}{\partial t} + \nabla \cdot \left(\alpha_f \mathbf{u}\right) = 0 \tag{4}$$

$$\frac{\partial \left(\alpha_f \mathbf{u}\right)}{\partial t} + \nabla \cdot \left(\alpha_f \mathbf{uu}\right) = -\alpha_f \nabla \frac{p}{\rho_f} - \mathbf{R}_{pf} + \nabla \cdot \tau \tag{5}$$

where α_f is the volume fraction occupied by the fluid, and its density is ρ_f ; $\mathbf{u}$ is the average velocity of fluid in a cell; p and τ represent the pressure and stress tensor in the cell. $\mathbf{R}_{pf}$ is the exchange of momentum with the particulate phase, which can be calculated by the particle-based drag force and is expressed as:

$$\mathbf{R}_{pf} = \frac{\left|\sum F_i^{f}\right|}{V_{cell} \cdot \left|\mathbf{u} - \langle v_p \rangle\right|} \left(\mathbf{u} - \langle v_p \rangle\right) \tag{6}$$

where V_{cell} is the volume of a CFD cell; $\langle v_p \rangle$ is the average velocity of the particles in the cell.

2.2.3 Fluid-particle interaction forces

The dominant fluid-particle interaction forces should be chosen depending on the different flow conditions so that some negligible items can be excluded and the problem can be simplified.

For a case where the mass ratio of two phases is small enough (e.g., $m_f \ll m_p$), neglecting other forces except drag force and pressure gradient force is reasonable and time-saving for analysis. Thus, the particle-fluid interaction force F^f is calculated as:

$$F^f = F_{\nabla p} + F_D \tag{7}$$

The pressure gradient force is defined as $F_{\nabla p} = -V_p \nabla p$, where V_p is the volume occupied by the solid phase and ∇p is the average local pressure gradient.

Different drag force (F_D) models for individual nonsphere particles were proposed in the past (Chien, 1994; Ganser, 1993; Loth, 2008; Thompson and Clark, 1991). When considering a practical particle dense flow such as the situation in this study, drag force has to be corrected over the single-particle laws based on some parameters such as local voidage and Reynolds numbers (Di Felice, 1994; Ergun, 1952; Wen and Yu, 1966). It should be pointed out that there is still no consensus up to now as to the perfect model to calculate the particle-fluid interaction drag force even in sphere particles dense flow, let alone the nonsphere particles (Zhong et al., 2016). Although it lacks a definitely accurate drag force model for nonsphere particles dense flow, some well-known equations can still be applied to CFD-DEM simulations (Adema et al., 2010; Hilton et al., 2010; Hilton and Cleary, 2011; Kuang and Yu, 2011; Liu et al., 2020b; Oschmann et al., 2015, 2014; Ren et al., 2013, 2012; Zhou et al., 2011). The drag force model developed by Lu and Gidaspow (LU and Gidaspow, 2003) for nonsphere particles dense flow is adopted in this study, which was developed based on the study of Ergun (Ergun, 1952) and Wen and Yu (Wen and Yu, 1966). Ergun firstly proposed a drag force model for relatively high particle concentration ($\alpha_s > 0.2$). Subsequently, Wen and Yu modified the theory for relatively low particle concentration ($\alpha_s < 0.2$). Lu and Gidaspow then applied a blending function to make the transition between Ergun and Wen in a smooth way and has been widely accepted (Adamczyk et al., 2014; Almuttahar and Taghipour, 2008; Wang et al., 2012). The model is expressed by:

$$\mathrm{F}_D = \frac{1}{2} C_D \rho_f A' \left|\mathbf{u} - \mathbf{v}_p\right| \left(\mathbf{u} - \mathbf{v}_p\right) \tag{8}$$

where $\mathbf{u} - \mathbf{v}_p$ is the relative velocity between particles and fluid; ρ_f denotes the density of the fluid; A' is the particles' projected area in the flow direction; C_D is the corrections of drag coefficient calculated based on the Reynolds number $Re_p = \rho_f \left|\mathbf{u} - \mathbf{v}_p\right| d_p / \mu_f$, d_p is the equivalent sphere diameter of the particle, and the μ_f is fluid viscosity. C_D is in the expression as:

$$C_D = \psi\left(\frac{200\alpha_s}{\alpha_f \phi^2 Re} + \frac{7}{3\phi}\right) + (1-\psi)\alpha_f^{-1.65} \max\left\{\frac{24}{\alpha_f Re_p}\left[1+0.15\left(\alpha_f Re_p\right)^{0.687}\right], 0.44\right\} \qquad (9)$$

where the ϕ is the sphericity of the nonsphere particle, representing the ratio of the actual area of the particle A_{p} and the equivalent area A_{equ} of a sphere having the same volume with the particle; α_s is a parameter to measure particle concentration; ψ is a function of the liquid volume fraction α_f.

2.3 Coupling procedure

The coupling procedure between the particles and fluid is realized by a staggered scheme that enables the parallel calculation of DEM and CFD. Once the kinematics of DEM is updated, these dates are submitted to the CFD to provide a solid fraction and assemble momentum for solving the locally averaged Navier–Stokes equations, and CFD transfers back the drag force and pressure gradient force to the DEM as part forces acting on the particles. DEM recalculates the contact forces and motions of particles for the next simulation loop. The flowchart of the coupling is shown in Fig. 4.

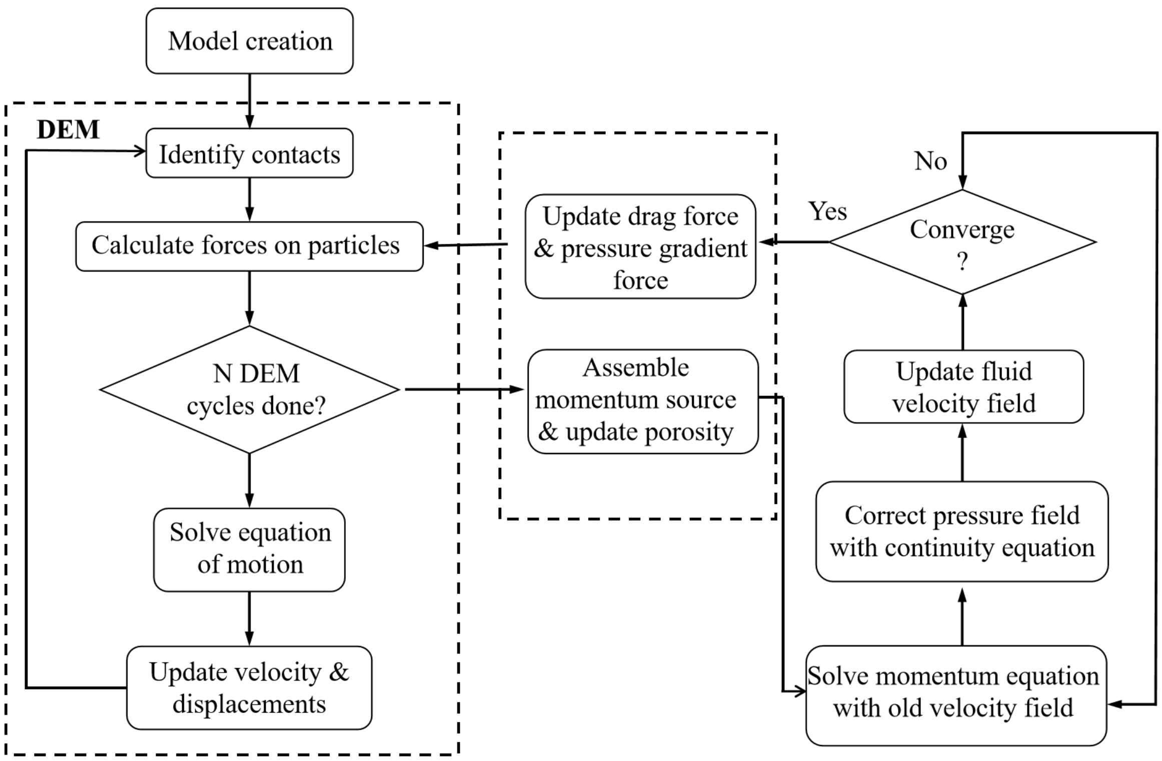

Fig. 4 Computational Computational fluid dynamics and discrete element method (CFD-DEM) coupling

scheme

3 Verification of the models

Since the quasi-spherical polyhedral particle is newly implemented in CFD-DEM coupling, the Ergun test (Ergun, 1952), which describes the fluid flow through a particle column, is examinend to verify the models. As shown in Fig. 5, the particles are deposited at the bottom of the cube due to gravity, and then fluid flows upward into the particle column at a constant superficial velocity v_s, resulting in a pressure drop between the inlet and outlet (for presentation purposes, the particle column is rendered separately on the left). According to the analytical solution of Ergun, the pressure drop Δp is a quadratic function of the superficial velocity, which can be described by the following expression:

$$\Delta p = \frac{150\mu L(1-e)^2}{d^2 e^3} v_s + \frac{1.75 L\rho(1-e)}{de^3} v_s \left| v_s \right| \tag{10}$$

where Δp is the pressure drop between the fluid inlet and fluid outlet; L=0.0156m denotes the particle bed length, d=0.001m is the particle diameter, and fluid density ρ is 1000kg/m^3. Dynamic viscosity μ is 1.5×10^{-3} Pa, and the void ratio of particle column e is 0.45. According to Ergun, once the superficial velocity v_s reaches the minimal fluidization velocity v_{mf}, the particle packing will fluidize and the pressure drop will no longer vary despite the increasing of superficial velocity. The coefficients in Eq.(10) were obtained by the method of least squares based on 640 experimental results (Ergun, 1952).

It should be noted that the shape effect is taken into account in CFD drag force calculations of nonspherical particles by introducing the correction of the drag coefficient C_D based on the sphericity (see Eq.(9)). As mentioned before, the particle shape adopted in this paper is quasi-spherical polyhedral, which is generated from a standard sphere, indicating that the non-convexity and eccentricity are neglected so as to highlight the angularity difference. Therefore, the difference in the sphericity of quasi-spherical polyhedral used to calculate the drag force is slight (the sphericity of these models is illustrated in the Table.1). In other words, the fluid-particle interactions should be close to each other according to the current drag force model. By introducing a quasi-spherical particle shape, it is possible to ensure that the current model for drag force calculation is still applicable while at the same time taking into account the influence of angularity on the interparticle contact during suffusion.

To calibrate and verify, the Ergun tests of spherical and quasi-spherical polyhedral particles with the angularity of 0.0099 and 0.0902 are simulated. Fig.6 shows a good agreement between these simulations and the analytical solution. The consistency of the results of sphere particles and the Ergun equation (Eq.(10)) verifies the accuracy of the coupled CFD-DEM method used in this paper. Furthermore, the results of Model 1 (correspond to the maximum angularity 0.0902) and Model 6 (correspond to the minimum angularity 0.0099) are only somewhat different from those of the sphere at v_s=0.014m/s. The pressure drop at the rest of the velocities and the maximum pressure drop after fluidization are similar to those of the sphere, indicating that current drag force model is suitable to quasi-spherical polyhedral particle.

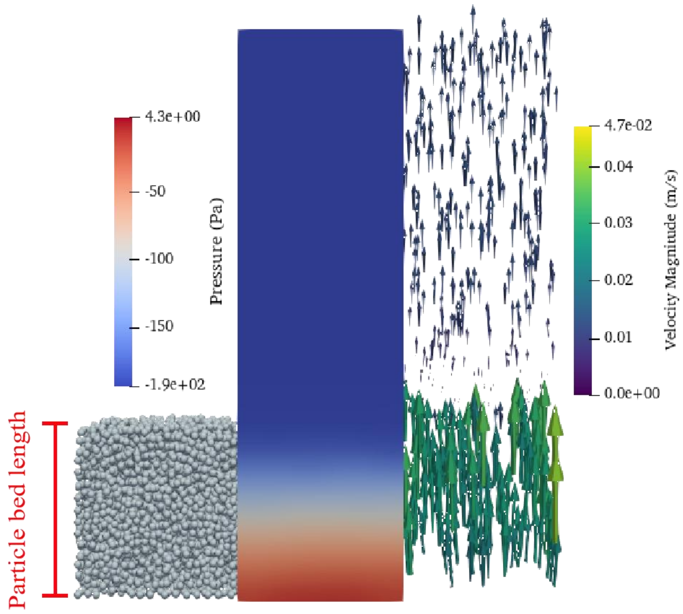

Fig. 5 Illustration of Ergun test.

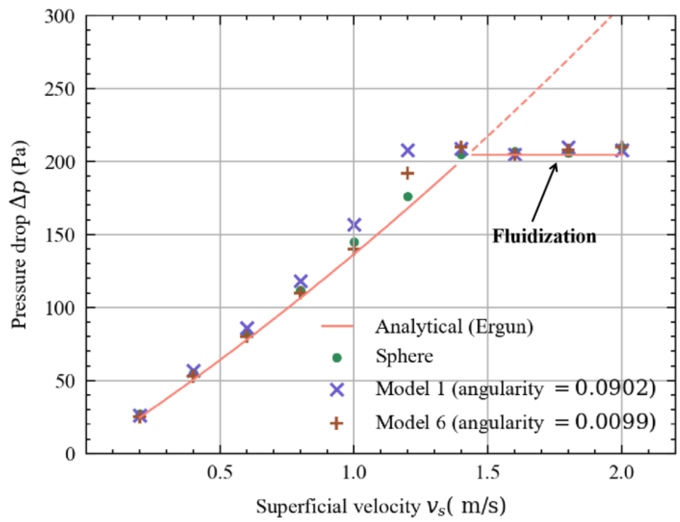

Fig. 6 Comparison of the Ergun test results of different particle shapes against the analytical solution.

4. Simulation Procedure

4.1 Particle preparation and model setup

The nonsphere particle adopted in this study is a quasi-spherical polyhedron with *n* vertexes. As illustrated in Fig.1, the particle with fewer vertexes will have many sharp protrusions on the surface and a larger angularity. To quantify the difference of these shapes, the angularity is taken as a dimensionless index defined as the ratio of particle's sphericity ϕ (the definition of sphericity see the Eq.(9)) and the number of its vertexes *n* (i.e., angularity=$\frac{\phi}{n}$). Table 1 lists the calculated angularity of the models in the simulation.

The gap-graded soils consist of two groups of particles, i.e., coarse particles $(D_c = 1.8 \sim 2\text{mm})$ and fine particles $(D_c = 0.3 \sim 0.33\text{mm})$. According to Kenney and Lau (Kenney et al., 1985), when the particles finer than *d* occupy a larger content proportion than the particles of grain size from *d* to 4*d*, the fines would likely be eroded. The index ratio d_{15} / D_{85}, where d_{15} the particle size of 15% mass passing in the fine fraction and D_{85} the particle size of 85% mass passing in the coarse fraction, is considered as an accessing criterion (Sherard et al., 1984). If $d_{15}/D_{85} > 4$ the soil is deemed internally unstable (Fannin and Moffat, 2006; Kenney et al., 1985) and suffusion erosion would be triggered once the external disturbance (e.g., hydraulic force) happens. Therefore, a gap-graded specimen consisting of more than 50000 particles with fines content $FC = 25\%$ in mass and $d_{15} / D_{85} = 6$ is generated. The grain size distribution (GSD) of the specimen is presented in Fig. 7.

Table 1. Angularity of particles

	Corners Number	Sphericity	Angularity
Model 1	10	0.9024	0.0902
Model 2	15	0.9351	0.0623
Model 3	25	0.9663	0.0397
Model 4	40	0.9790	0.0245
Model 5	60	0.9870	0.0165
Model 6	100	0.9918	0.0099

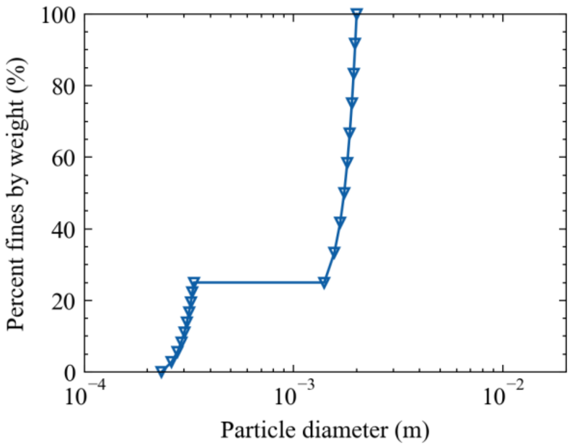

Fig. 7. Grain size distributions of gap-graded granular material in numerical simulations

The sample is modeled as a cuboid with a size of 16mm×16mm×16mm. The size ratio between cube length and maximal coarse particles is set to 8 to eliminate the border effect (Hu et al., 2020, 2019; Liu et al., 2020a; Xiong et al., 2020). The CFD domain overlaps the DEM with the size of 16mm×16mm×20mm with an extra in height, ensuring the flow covering soils entirely. The fluid is decomposed into 2mm×2mm×2mm cells, approximately six times the fine particle diameter (0.3mm). By controlling the motion of six surrounding rigid walls, stress and strain can be imposed on the sample. In the process of suffusion, the top wall is considered to be permeable, whereas the other four upright side walls are impermeable so that a one-way fluid flows from bottom to top through the solid fractions. The determination of upward seepage direction is referred to previous experiments (Hu et al., 2019; Tao and Tao, 2017; Tomlinson and Vaid, 2000). Only the friction between particles is counted, and the friction coefficient between the particle and wall is zero. The Young's modulus has a significant influence on the determination of time step and particle overlapping, while the value of the modulus varies over a wide range in the existing studies (Chang and Zhang, 2013; Liu et al., 2020a; Xiong et al., 2020). Following Chand et al. (2012), the magnitude is chosen as 1×10^8 Pa to ensure the sum overlap is smaller than 2%. The time step equals 2×10^{-5} s in the CFD domain, corresponding to 100 times that of the DEM. Other related parameters used in the paper are summarised in Table 2.

Table 2. Input parameters for suffusion erosion simulation

Parameter	Value	Unit
Particles		
Particle density	2650	kg/m^3
Young's modulus	1×10^8	Pa

Friction coefficient	0.5	
Restitution coefficient	0.3	
Timestep	2×10^{-7}	s
Diameter	0.3~0.33 1.8~2	mm
Poisson's ratio	0.3	
Gravitational acceleration	9.8	m/s^2
Walls		
Young's modulus	1×10^{10}	
Friction coefficient	0	
Restitution coefficient	0.3	
Hole size of the filter wall	0.75×0.75	mm
Fluid		
Cell size	2×2×2	mm
Fluid density	998	kg/m^3
Hydraulic gradient	4	
Timestep	2×10^{-5}	s

4.2.Simulation procedure

The simulation can be generalized into four stages:

Stage 1: Sample generation. A specific mass of non-overlapping particles is dispersed in a cube larger than the established size. A force acts on the walls to move them towards particles and gradually compact the sample. The gravity in this step is switched off to ensure homogeneity. Otherwise, the fines would accumulate at the bottom through the pores of large particles because of dead-weight. When the system is balanced, there is a 100kPa stress acting on the surrounding walls to consolidate the soils (as shown in Fig.8). According to Zhao et al. (Zhao et al., 2015), particle shape affects the inner fabric and alignment of particles, which are closely related to the void ratio in soils. Table 3 lists the initial void ratio after generation. At the same stress level, the initial void ratios are not exactly the same due to the variance of shapes.

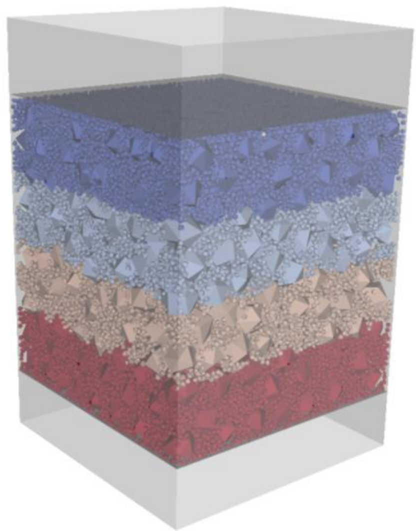

Fig. 8. Generated particle assembly.

Table 3. Details of Generated samples

	Angularity	Particle Numbers	Initial Void ratio
Model 1	0.0902	50590	0.418
Model 2	0.0623	50590	0.415
Model 3	0.0387	50574	0.394
Model 4	0.0245	50583	0.386
Model 5	0.0165	50594	0.378
Model 6	0.0099	50590	0.382

Stage 2: Gravity balance. Gravity in this step is switched on, leading to internal rearrangement of the sample. The balance stage lasts 2s, and then the top is replaced with a filter wall, which has filter holes of the size 0.75×0.75mm. The hole is 2.5 times the diameter of fines and is smaller than the coarse particles, ensuring the flow can smoothly carry away the fines, and the coarse particles are blocked.

Stage 3: Suffusion erosion. The coupling of the DEM and CFD starts from this stage. Fluid flows at a constant hydraulic gradient, and interaction forces come into play. Fines are taken away through the voids of the coarse matrix. Once the fines rush out of the filter, they will be deleted by the DEM domain, resulting in mass loss. The coupling process lasts 10s (Fig. 9). The four sidewalls and the top filter wall keep fixed, whereas the bottom wall keeps a constant stress level of 100kPa.

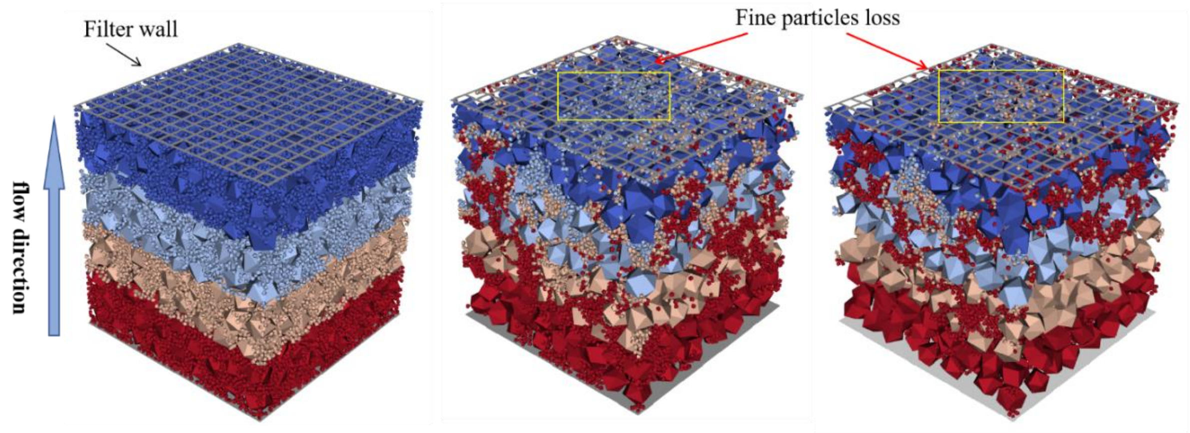

(a) (b) (c)

Fig. 9. The seepage development process. (a)time=0s; (b)time=5s; (c)time=10s

Stage 4: Triaxial test. Triaxial tests are carried out on the post-eroded specimens under strain loading, where the largest axial strain is set to 20% with confining stress of 100kPa (as shown in Fig. 10). Also, the sample that didn't undergo the suffusion erosion (e.g., skipping stage 3) will be loaded to explore the effect of both erosion and angularity on mechanical property.

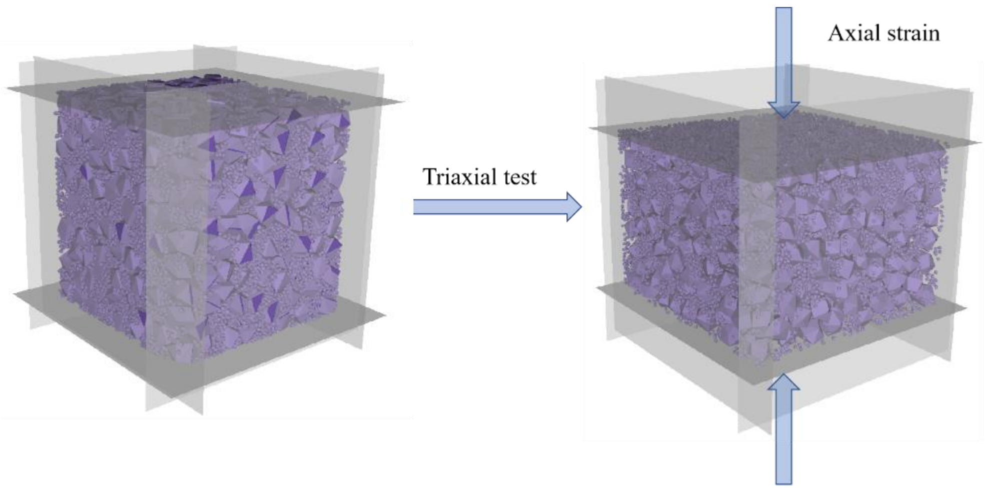

Fig. 10. Schematic diagram of stress servo-control triaxial test

5.Results analysis

5.1 Analysis of the macroscopic behaviors

5.1.1 Fines loss

Fines mass loss ratio m_e, defined as the cumulative fine loss normalized by the total fine mass ($m_e = \frac{\text{eroded fine mass}}{\text{total fine mass}}$), is an essential parameter to quantify suffusion erosion. Fig. 11 plots the cumulative mass loss versus time. In the first two seconds, the fines loss is rapid, and then it starts to slow down in the sample with a relatively large angularity (see Model 1 to Model 3, the corresponding angularities are 0.0902, 0.0623, 0.0387). Conversely, there is a turning point in the samples with a relatively small angularity (Model 4 to Model 6), from which the rate of fines loss is again accelerated (the corresponding turning points for Model 4, Model 5, and Model 6 are 7.6s, 3.8s, and 7.8s). By comparing the cumulative mass loss ratio at 10s, we can find that the results corresponding to different angularity vary notably. Generally, the ultimate erosion fines ratio increases significantly as the angularity decreases. For example, the value of Model 1 (the angularity of particle is 0.0902) is 31.8%, while that of Model 6 (the angularity of particle is 0.0902) doubles up to 65.7%. This phenomenon suggests that particles with large angularity are more resistant to erosion by fluids. Zhao et al. (2015) point out that a self-locking effect is formed between the polyhedral particles, increasing particle-to-particle occlusion, resulting in strong resistance to the fluid. Coarse particles are not easily migrated due to the angularity enhancing the self-block effect. As a result, fines can hardly traverse soil skeletons.

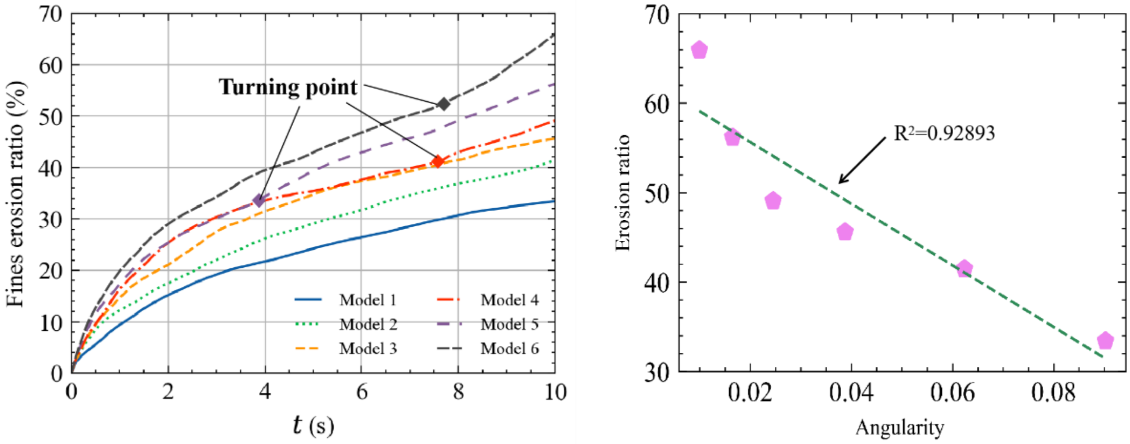

(a) (b)

Fig. 11. Evolution of fines mass loss: (a) cumulative fines erosion ratio; (b) ultimate eroded mass

To further reveal the relationship between ultimate fines mass loss and angularity, the two are simply linear fitted in Fig. 11(b). There is a negative correlation between them. Especially when the angularity is in the range of 0~0.03, the fines mass loss ratio has a sudden drop with angularity increasing. In addition, Fig. 12 also plots the comparison of the grain size distributions (GSD) after the models have undergone suffusion. Fines content decreases with the decline of particle angularity, reminding that suffusion erosion leads to a vital transformation in the soils' initial state.

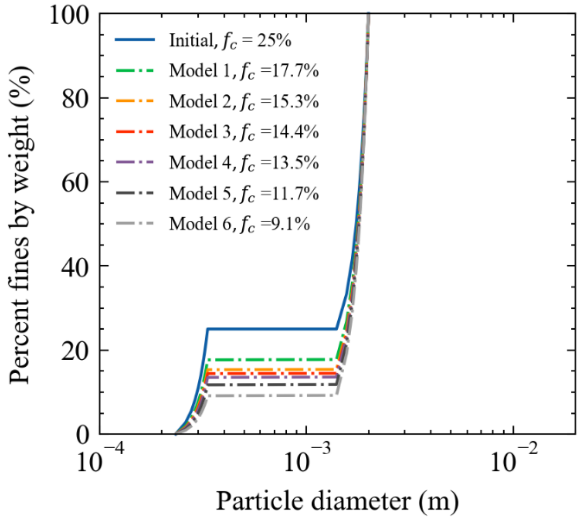

Fig. 12. Grain size distributions of models after erosion

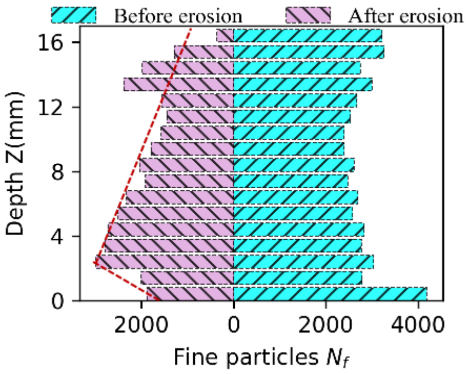

(a) Model 1

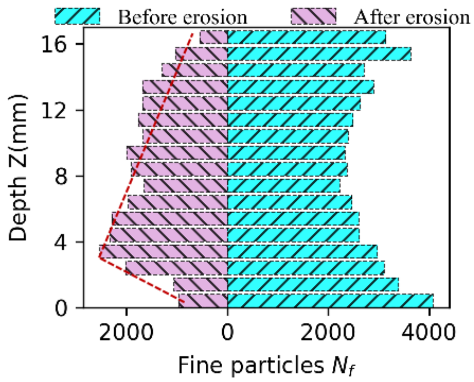

(b) Model 2

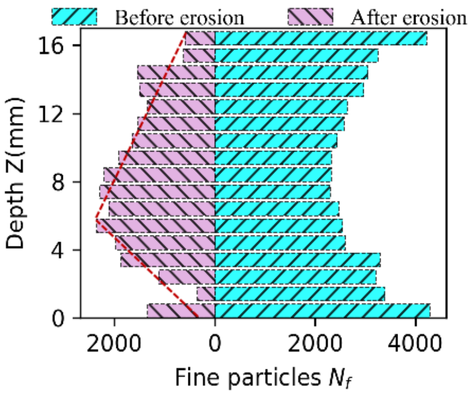

(c) Model 3

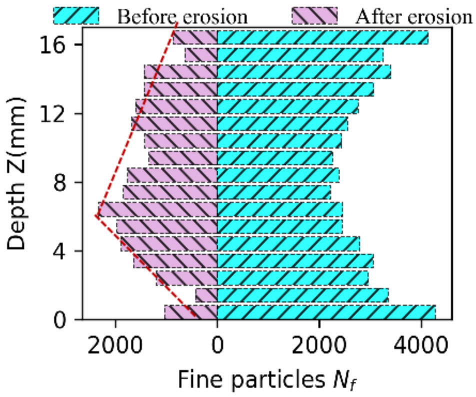

(d) Model 4

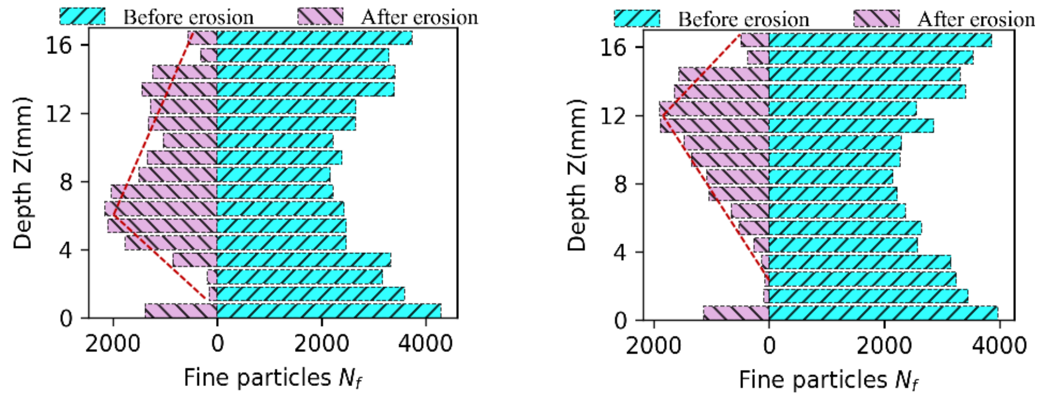

(e) Model 5 (f) Model 6

Fig. 13 Comparison of fine particle distribution along depth Z at the state before and after erosion

Fig. 13 plots the distribution of fines along the seepage direction. The depth represents the distance from a point to the bottom of the specimen. Firstly, the distribution of fine particles before erosion is relatively uniform along with the depth, indicating that the aforementioned specimen generation method in stage 1 is suitable. However, after erosion, a triangle-like distribution is presented. The number of fines at the ends drops abruptly compared to the pre-erosion, while that of fines located in the middle part of the specimen does not change significantly, showing that the fines are clogged in the midst. This phenomenon is also observed by Xiong et al. (2020). The result is explained as follows: the seepage path of the fine particles near the filter wall is short. Consequently, these particles are easily eroded away under the fluid-particle interaction force. The further away from the filter wall, the more likely it is that particles will be clogged, so many fines are blocked in the middle of the specimen, which can also be seen from the variation of void ratio (Fig.14). The void ratio of the top layer (H5 and H6 in Fig.14) and the bottom layer (H1 and H2 in Fig.14) varies dramatically (due to the small amount of fines loss in Model 1, the variation of the bottom layer void ratio is not very significant). In contrast, the middle layer (H3 and H4) changes relatively more smoothly.

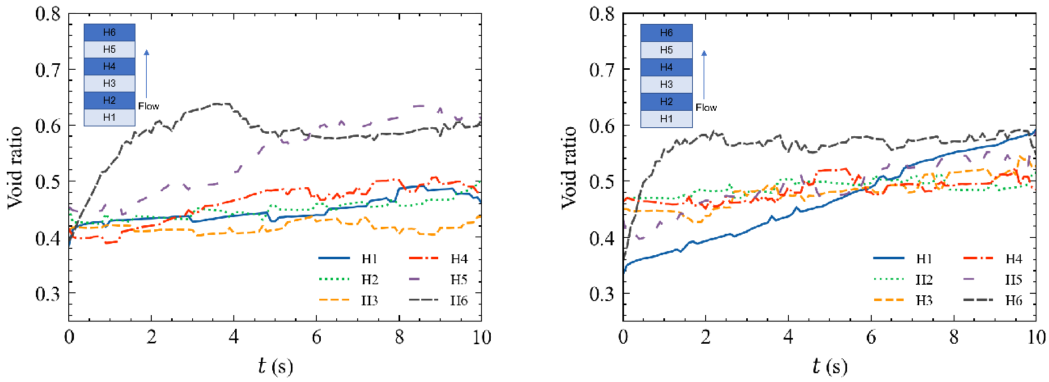

(a) Model 1 (b) Model 2

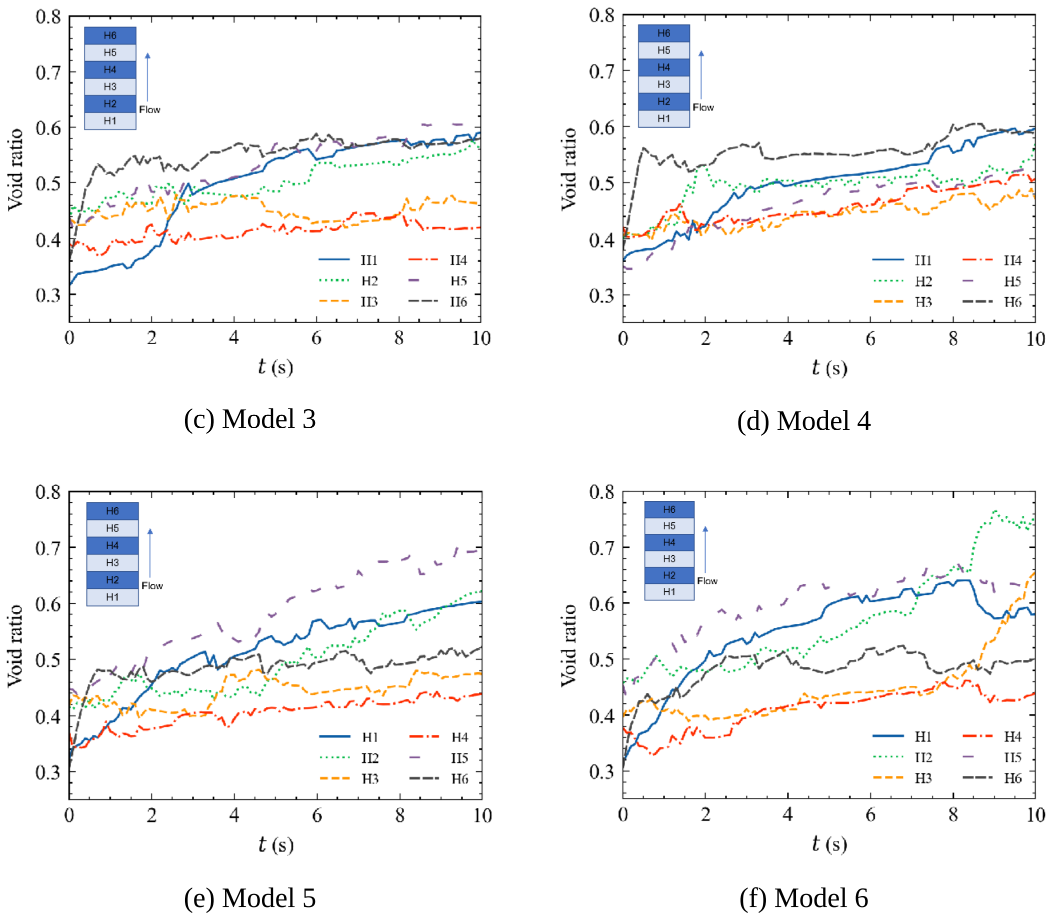

Fig. 14. Evolution of void ratio in different layers.

5.1.2 Vertical displacement

The fluid is considered as upward flow, i.e., seepage direction opposite the direction of gravity, and the top filter wall maintains stationary, which is consistent with laboratory tests (Shi et al., 2018; Tomlinson and Vaid, 2000). Only the bottom wall moves upward under a fixed 100kPa stress due to the loss of particles. The amount of upward displacement of the bottom wall can be considered vertical displacement.

Erosion-induced settlement in the six models is plotted in Fig. 15. A distinctive feature is that settlement variation with time can be divided into two or three phases: (1) Acceleration phase: during this process, the surface settles rapidly. This is mainly due to the loss of the fine particles initially close to the filter wall. Each model goes through this phase, but they do not last the same amount of time. For example, the accelerated loss phase of Model 6 lasts until about 1.6s, but the curve of Model 1 does not gradually start to level off until about 7.2s. (2) Metastable phase: In this phase, the fine particles far from the filter wall have a long percolation path, and the angularity of particles makes their percolation path not smooth. Consequently, the loss of fines slows down. Since the external loads acting on the soil are mainly carried by the soil skeleton formed by coarse particles, and the accumulated fines loss at this phase is not enough to destabilize the current skeleton, thus the settlement throttles. Even though a displacement surge occurs at some moments, the magnitude of the increase is small, indicating that the soil skeleton is only locally adjusted at this time and that there is no overall redistribution of the coarse particles. For example, Model 3 has a step increase at 4.6s and 8.3s, respectively, but the duration of this surge is short, and the displacement settlement is not significant. Therefore, Model 3 is still considered to be in the metastable stage during 2.7-10s. (3) Soil skeleton redistribution phase: This phase only occurs in Model 6 (as shown in Fig. 15, three phases of Model 6 are delineated by the dash line). Due to the small angularity in Model 6, the particles are prone to misalignment with each other. In addition, the severe fines loss makes the metastable structure destroyed, and the coarse particles undergo redistribution, as a result, surface displacement increases sharply.

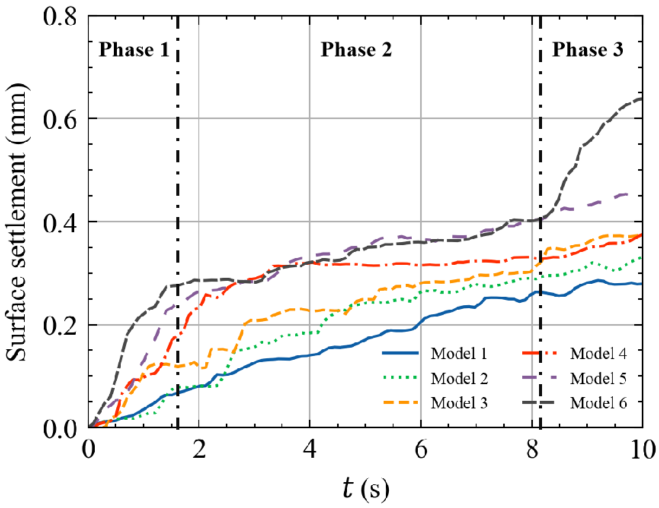

Fig. 15. Temporal evolution of vertical displacement;

Fig. 16 plots the vertical displacement field inside the specimen after suffusion. For presentation purposes, the fines are set in gray, and only the displacement field of the soil skeleton (i.e., coarse particles) is highlighted. Because the top wall is set as a fixed boundary during suffusion and the bottom wall maintains a stress servo, the loss of fines will lead to upward displacement of the bottom wall and, as a consequence, a large displacement of coarse particles at the bottom of the specimen will follow. The closer the particles are to the top, the smaller the displacement will be. Besides, the increase of the angularity can effectively restrict the particle displacement. For example, the percentage of small-displacement particles (in dark color) in model 1 is greater than that in Model 6. Simultaneously, the maximum displacement in Model 6 (the angularity is 0.0099) is 0.638mm, larger than the maximum displacement of 0.286mm in Model 1 (the angularity is 0.0902).

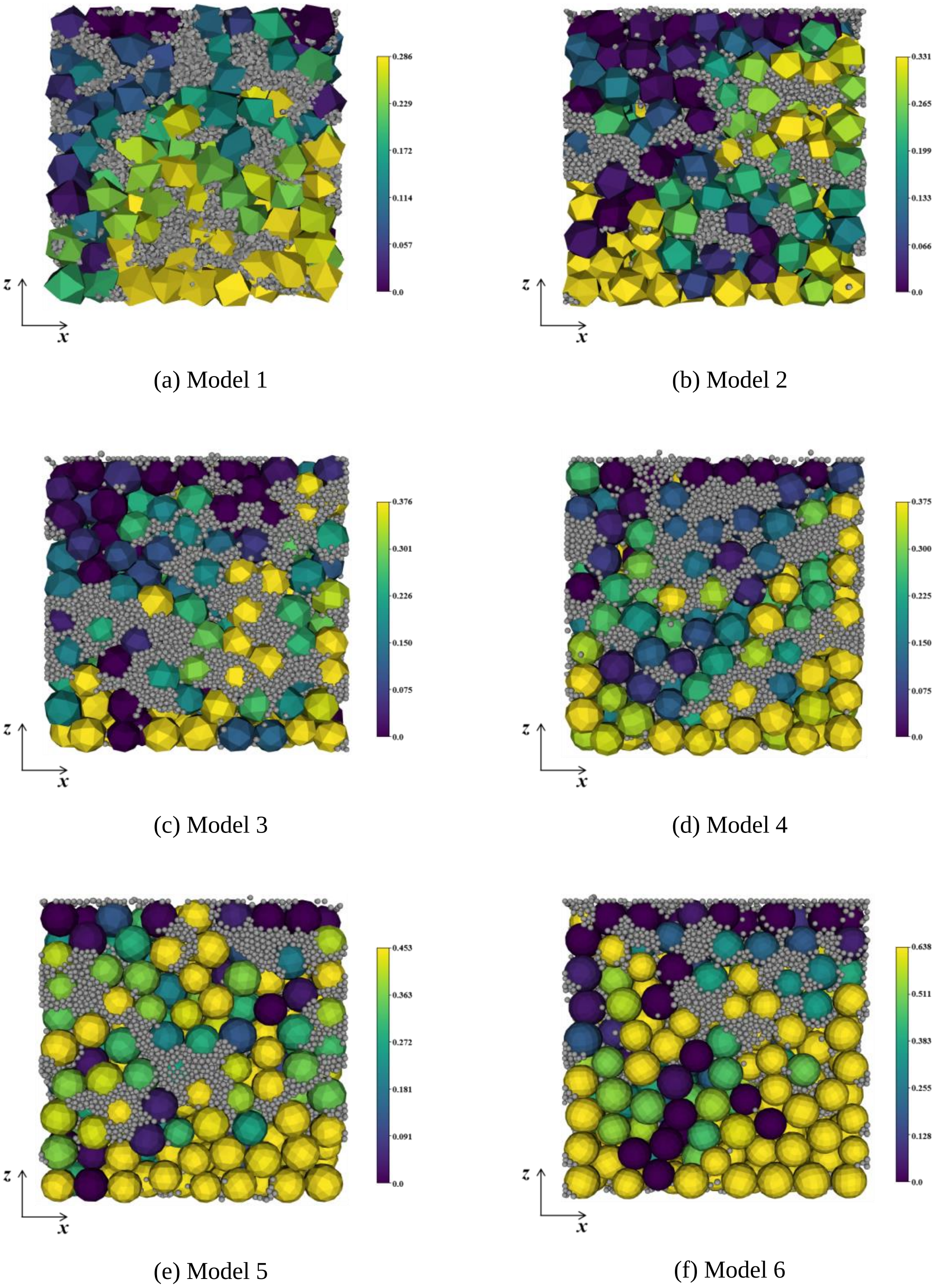

Fig. 16 Vertical displacement field

5.1.3 Volume flow rate

Suffusion erosion involves complicated solid and fluid interaction. Thus the liquid phase would also be affected due to the loss of particles. The volume flow rate Q is introduced to reflect the behavior of the water flow. Volume flow rate Q is defined as $Q = v \cdot A$, where v is the velocity of flow and A is the cross-sectional vector area (in this paper, A is the area of filter wall). Fig. 17 plots the evolution of volume flow rate versus erosion time, from which we can find that at the beginning of the simulation, the value of the rate is relatively small (approximately $2.5\times10^{-6}m^3/s$). At this moment, the permeability of the specimen is poor, and the hydraulic conductivity k is very small. Therefore, the velocity of flow is slow at a given hydraulic gradient ($v = k \cdot i$). With the development of erosion, the volume flow rate gradually increases, indicating that the samples tend to be loose and more permeable to water. In addition, the smaller the angularity, the more serious the loss of fines (Fig. 11) and the greater the volume flow rate (Fig. 17). Specifically, the significant fines loss in Model 6 leads to a considerable void ratio variation and the permeability of the specimen increases. As a result, the volume flow rate in Model 6 is more prominent than in others. The consistency of particle transport and fluid transmutation confirms the effectiveness of the coupled CFD-DEM method used in this paper.

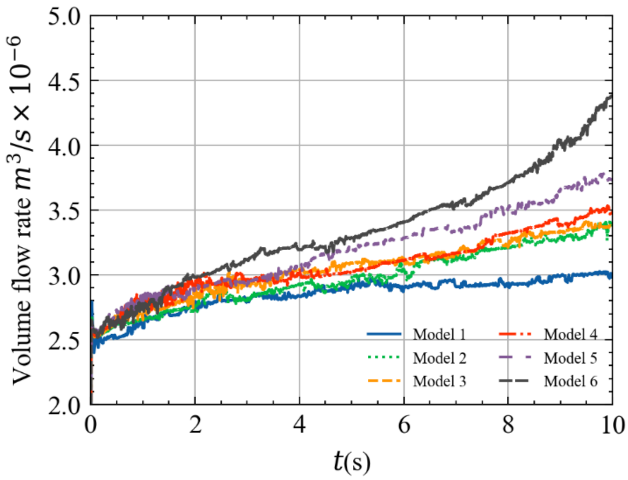

Fig. 17. Volume flow rate versus time

5.1.4 Mechanical behavior of pre-and post-eroded soils

Fig. 18 plots the stress ratio and volumetric strain versus the axial strain for the virgin sample (i.e., without suffusion) and eroded ones in different angularity. Stress ratio(q/p) is defined as the ratio of deviatoric stress ($q = \sigma_1 - \sigma_3$) and mean effective stress ($p = (\sigma_1 + \sigma_2 + \sigma_3)/3$). As the applied strain increases, the stress ratio first gradually increases to a threshold and then decreases to the critical state. The corresponding volumetric deformation first decreases (i.e., shear shrinkage), followed by an increase in axial strain, and then dilatation occurs. Even when the soil underwent severe suffusion, the pore ratio has increased significantly, but the post-eroded samples still maintain the characteristics of strain-softening. By comparing the peak stress ratio of specimens with different angularity, it can be found that angularity facilitates soils' shear strength. As is illustrated in Fig. 19a, the peak stress ratio increases with increasing angularity. The peak stress ratio varies remarkably for the specimens with large angularity before erosion, whereas there is no significant difference in the peak stress ratio when the angularity is small. However, for the specimens after suffusion, there is a linear relationship between the peak stress ratio and the angularity. A similar phenomenon is also observed in the soil's friction angle (Fig. 19b), which is defined as $\varphi = \arcsin\left[\left(\sigma_1 - \sigma_3\right)/\left(\sigma_1 + \sigma_3\right)\right]$. The angularity enhances the self-locking effect (Zhao et al., 2015) between particles, and the rotational misalignment is thus suppressed. As a result, both the internal friction angle and shear strength of soil are intensified.

Due to the nonlinearity of the soil at the beginning of loading (Xiong et al., 2020), E_{50}, which is defined as the secant modulus corresponding to half of the peak stress, is introduced. Fig. 20 plots the E_{50} of both pre-eroded and post-eroded specimens. It can be observed that: (1) erosion causes a sudden decrease in soil stiffness E_{50} in Model 1~3; and (2) erosion has minimal effect on E_{50} in Model 4~6, and the post-eroded E_{50} is even improved compared to the pre-eroded soils. Actually, the particles in Model 1 are so closely aligned due to a large angularity that the soil skeleton hardly deformed under external loading. Therefore, the peak strength is not reached until the axial strain reaches about 13%, after which softening begins. Compared to Model 1, peak strengths of pre-eroded specimens of Model 2 and 3 do not decrease significantly. Nevertheless, they start to soften when the strains reach only about 8%, and their E_{50} increases instead. After erosion, the strength of soils decreases due to fines loss and readjustment of particle fabric, and E_{50} of Model 1-3 show different degrees of reduction. In Model 4-6, due to excessive fines loss and minor rolling resistance between particles, the soils form a sub-stable structure (Liu et al., 2020a; Xiong et al., 2020). This results in a decrease in their peak strength compared to the pre-eroded samples, but the E_{50} modulus is slightly larger than that before suffusion.

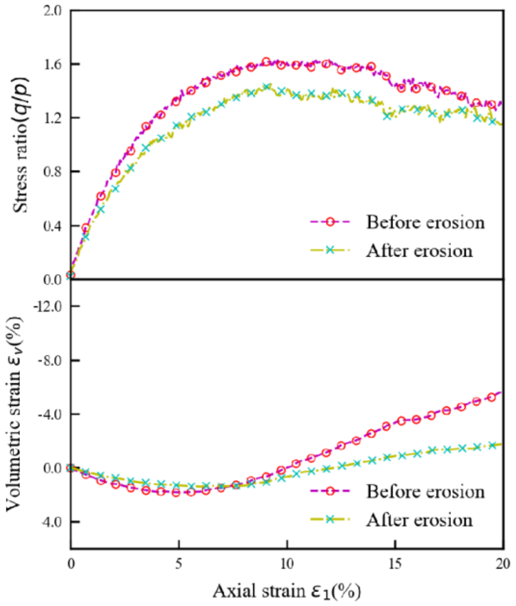

(a) Model 1

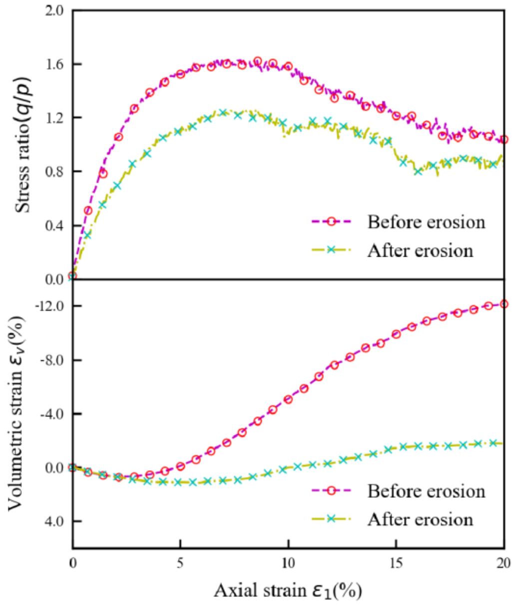

(b) Model 2

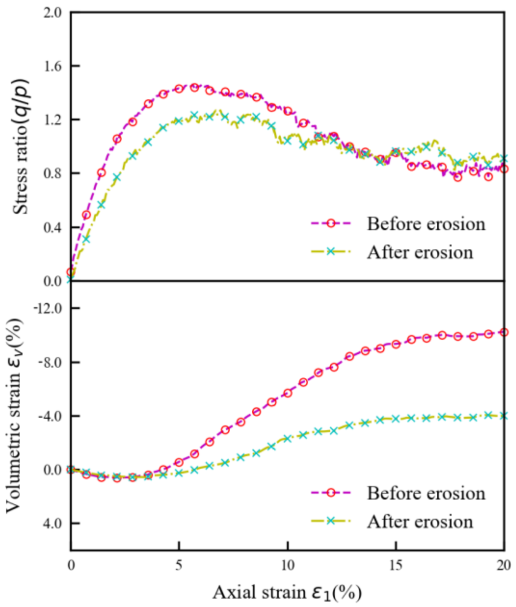

(c) Model 3

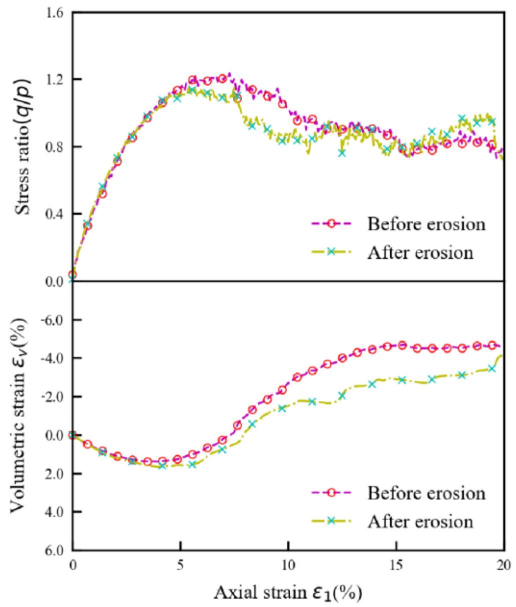

(d) Model 4

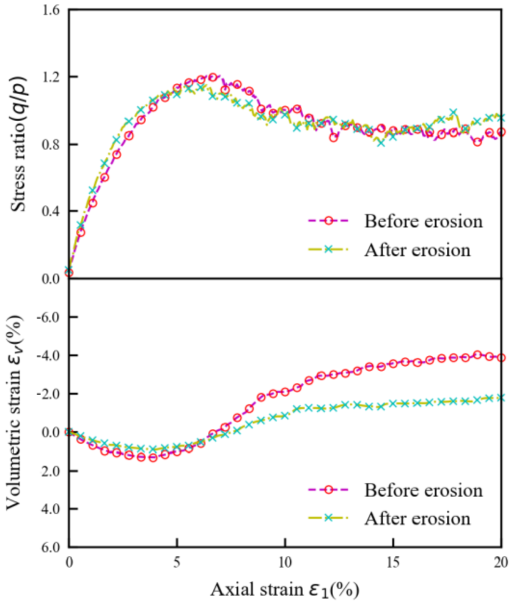

(e) Model 5

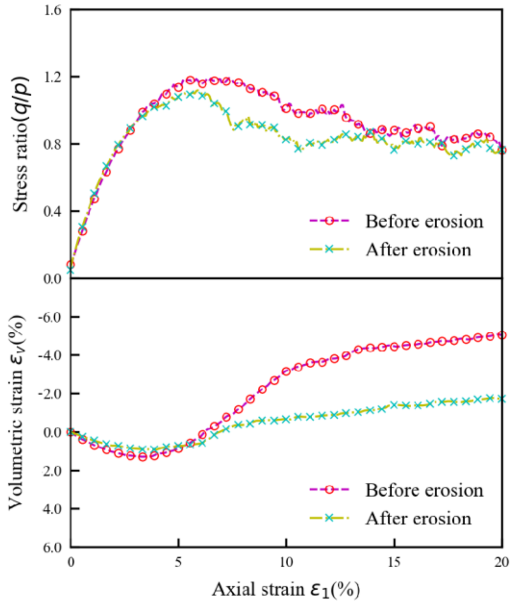

(f) Model 6

Fig. 18 Variation of strength and deformation characteristics expressed by stress ratio (deviatoric stress over mean effective stress) versus axial strain and volumetric strain versus axial strain.

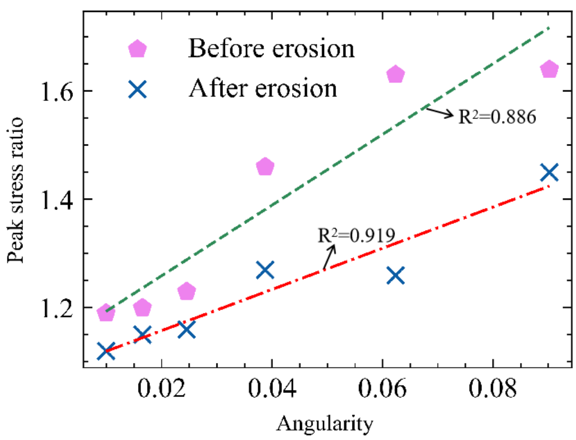

(a) Peak stress ratio variation versus angularity

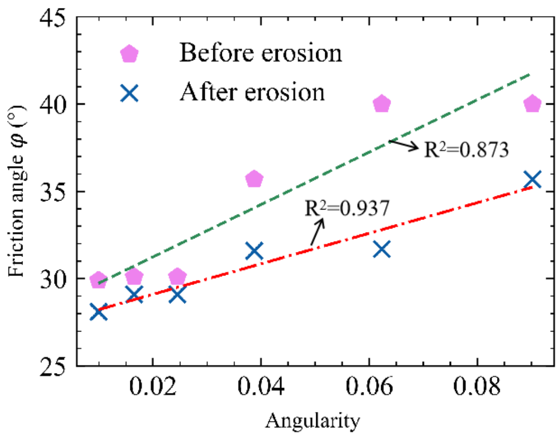

（b）Friction angle variation versus angularity

Fig. 19 Variation of peak stress ratio and friction angle versus angularity.

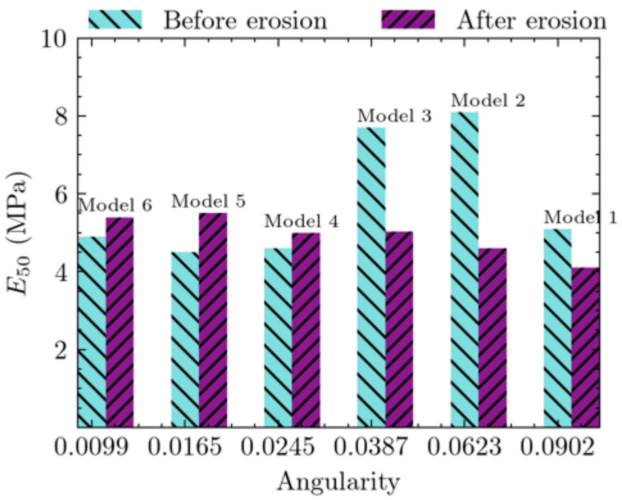

Fig. 20 E_{50} in different samples

5.2 Analysis of the microscopic behaviors

5.2.1 Strong force chains

A significant advantage of the discrete element method is to record and analyze forces and contact information for each particle, which facilitates the study of soil behavior from a microstructural perspective. Previous investigations show that the normal contact force has a more pronounced effect than the tangential contact force (Azéma et al., 2009; Thornton, 2000). The evolution of normal contact forces at the microscopic level can mechanistically explain some macroscopic phenomena.

Based on the size of the two particles, three types of contact are categorized: (1) c-c contact: the contact between coarse particle and coarse particle; (2) c-f contact: the contact between coarse particle and fine particle; (3) f-f contact: the contact between fine particle and fine particle. According to Azema and Thornton (Radjai et al., 1998; Thornton and Antony, 1998), force transmission is divided into two patterns: strong force contributes mainly to macroscopic deviatoric stresses, and weak force contributes mainly to isotropic stresses that maintain the stability of the strong force chain. Referring to the Minh et al. (Minh et al., 2014), the criterion for distinguishing between strong and weak forces is set to be $1.2\langle f_n \rangle$ in this paper, where $\langle f_n \rangle$ is the average normal force of all the contacts. The forces above $1.2\langle f_n \rangle$ are strong forces. On the other hand, those who less than $1.2\langle f_n \rangle$ are the weak forces.

Fig. 21 counts the strong force distribution in the three contact types of different angularity samples. The type of c-c and c-f contact dominates both pre-eroded and post-eroded specimens, implying that coarse particles are involved mainly in strong force chains. The proportion of strong force in f-f contacts decreases significantly with decreasing angularity (Fig. 21a). For example, their distributions in c-c and f-f contacts of Model 1 (the corresponding angularity is 0.0902) are similar, whereas, in Model 6 (the corresponding angularity is 0.0099), almost no strong force exists in f-f contacts. The phenomenon indicates that angularity favors the fine particles to bear greater contact forces, consistent with others' points (Zhao et al., 2015) that angularity intensifies the self-locking effect between particles. Fig. 21b illustrates the results of post-eroded specimens, from which we can find that as the angularity decreases, the proportion of c-c gradually increases, while that of c-f gradually decreases. However, it should be emphasized that the discrepancy in allotment of c-c and c-f is not remarkable before suffusion. This indicates that the angularity has little effect on the initial strong force distribution in c-c and c-f, whereas it has significant effects after erosion. The reason is that with the reduction of angularity, fines loss considerably proliferates, and the c-c contacts consequently create more strong force chains to bear forces.

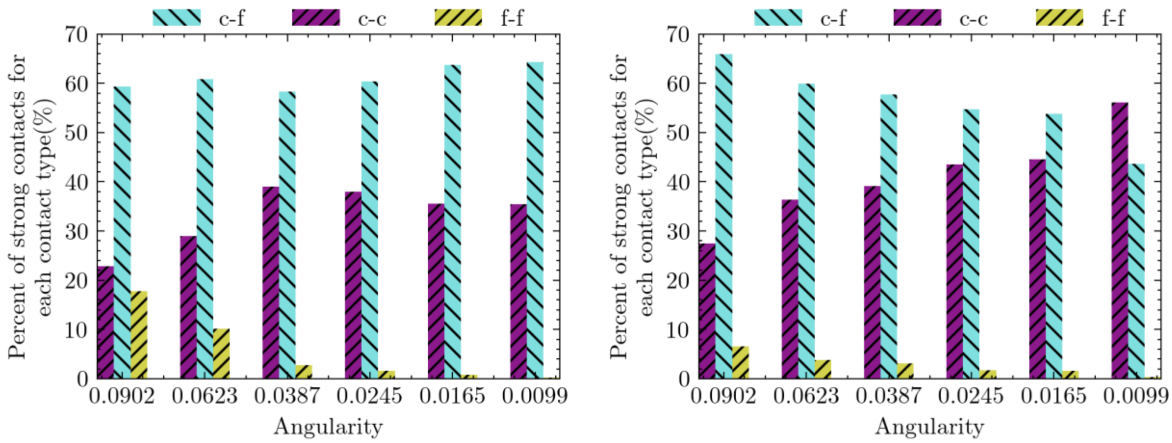

(a) Before erosion (b) After erosion

Fig. 21 Distribution of strong force chains in c-f, c-c, f-f contact types

5.2.2 Mechanical coordination number

Coordination number is defined as the number of particles touching with the neighboring particles. For the gap-graded soils, given that the particles having none or one contact barely contribute to force transmission, the mechanical coordination number Z_m exhibits a granular assembly structure more accurately (Thornton and Antony, 2000). Z_m is calculated as:

$$Z_{\mathrm{m}} = \frac{2C - N_1}{N - N_0 - N_1} \tag{11}$$

where N_0 and N_1 denote the number of particles with null and one contact, respectively; C is the total contact number in the assembly. Specifically, Z_m can be further classified into three types based on the contacts (Hu et al., 2020): the average contact number of c-c contacts per coarse particle $Z_{c\text{-}c}$, c-f contacts per particle $Z_{c\text{-}f}$, and f-f contacts per fine particle $Z_{f\text{-}f}$. The evolution of the mechanical coordination number in three different contacts is shown in Fig. 22. It's observed that the $Z_{c\text{-}f}$ is remarkably larger than $Z_{f\text{-}f}$ and $Z_{c\text{-}c}$, showing that many fines will be attached around coarse particles for gap-graded soils, raising the contacts between coarse and fine particles. What is more, $Z_{c\text{-}f}$ decreases, and $Z_{c\text{-}c}$ increases gradually with elapsed time. The tendency is more pronounced in the models with severe fines loss (e.g., Model 5 and Model 6). This indicates that fines loss leads to a reorganization of the internal structure, and coarse particles will create more contacts to maintain the stability of the soils that have weakened due to erosion. On the contrary, $Z_{f\text{-}f}$ remains almost constant. It is because that fines diffusing in the pores of coarse particles mainly play a filling role. The contribution of these particles in force transmission is tiny (Liu et al., 2020a; Minh et al., 2014).

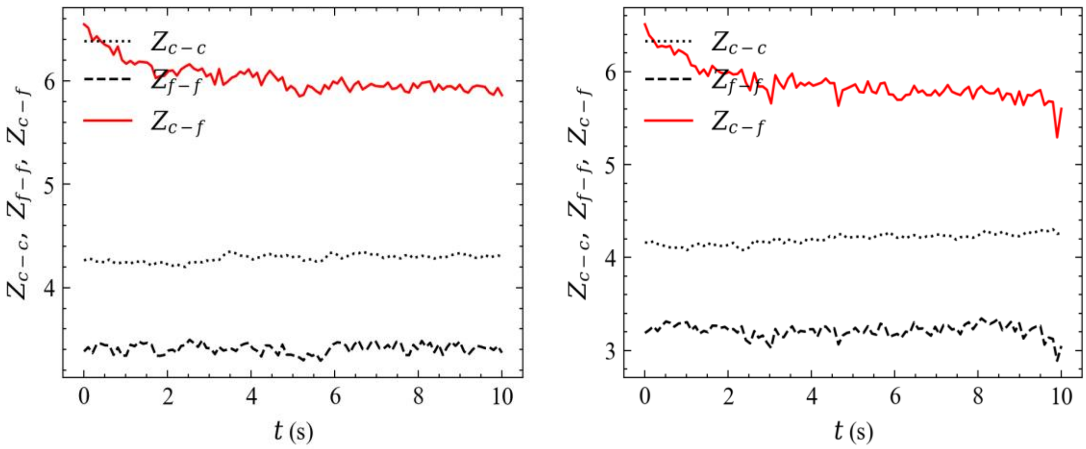

(a) Model 1 (b) Model 2

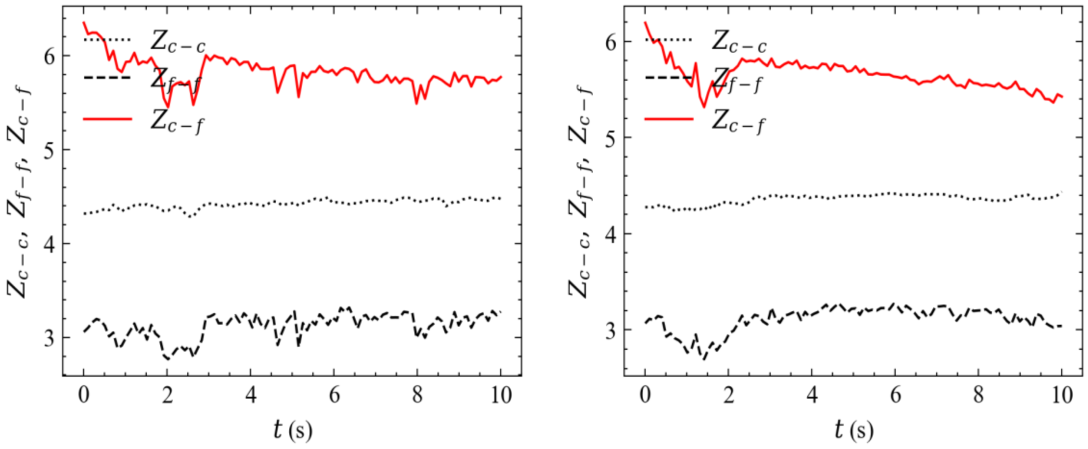

(c) Mode 3 (d) Model 4

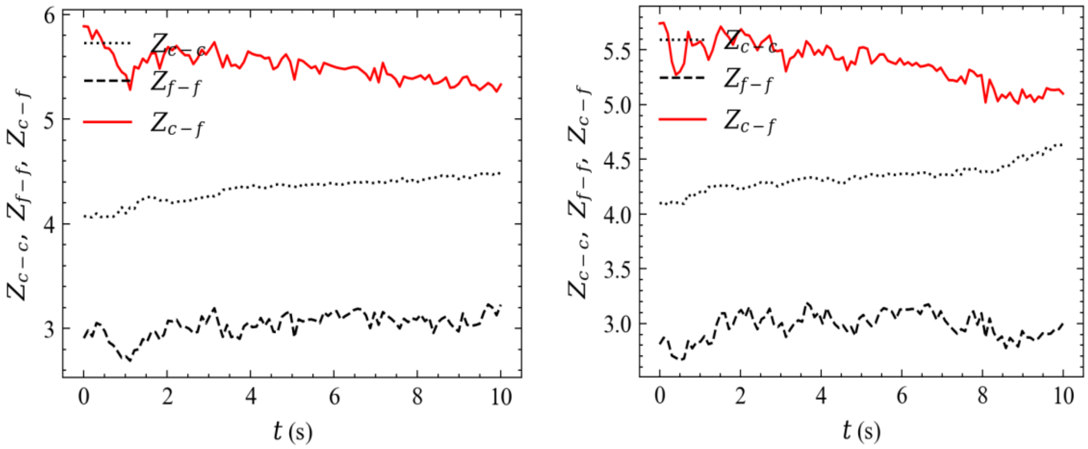

(e) Model 5 (f) Model 6

Fig. 22 Evolution of mechanical coordination numbers during suffusion.

5.2.3 Evolution of force network

The force network consists of two force categories (strong force and weak force) as mentioned above, which can be represented in the form of the force chain (as shown in Fig. 23). All the contact forces are presented by the cylinders linking the adjacent particles whose radius and colors represent the magnitude of the force.

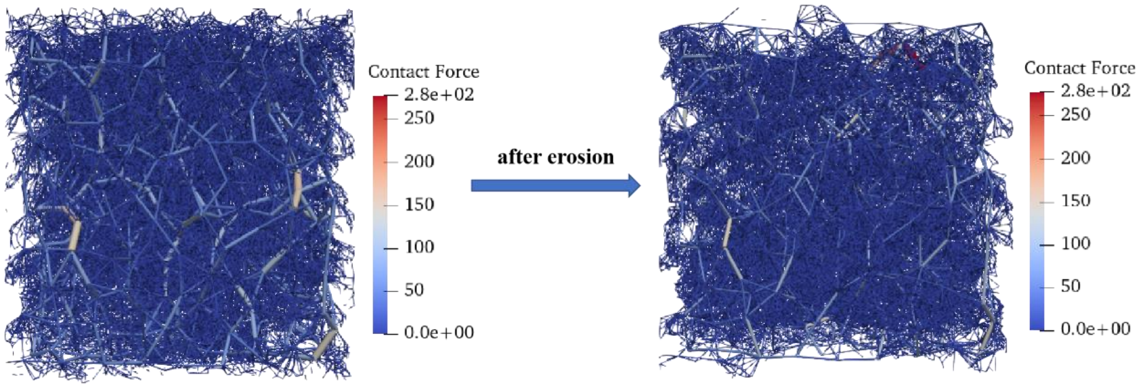

(a) Model 1

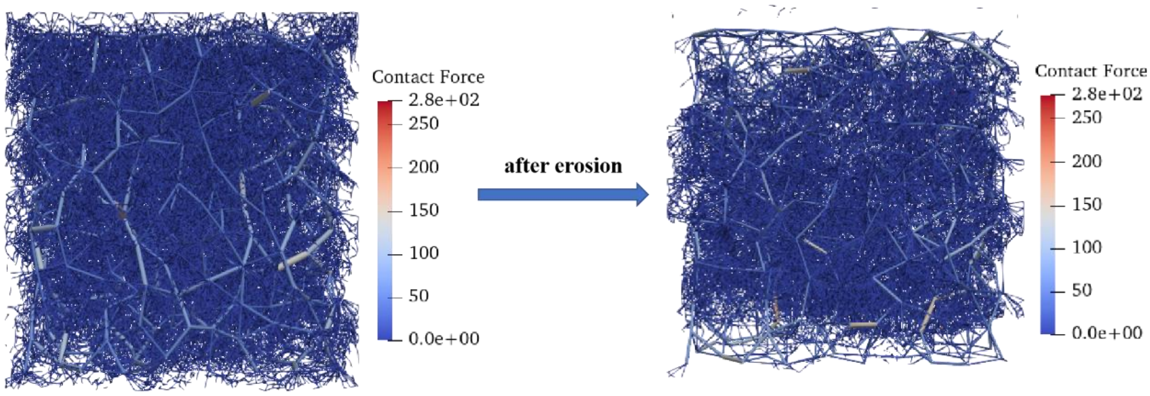

(b) Model 2

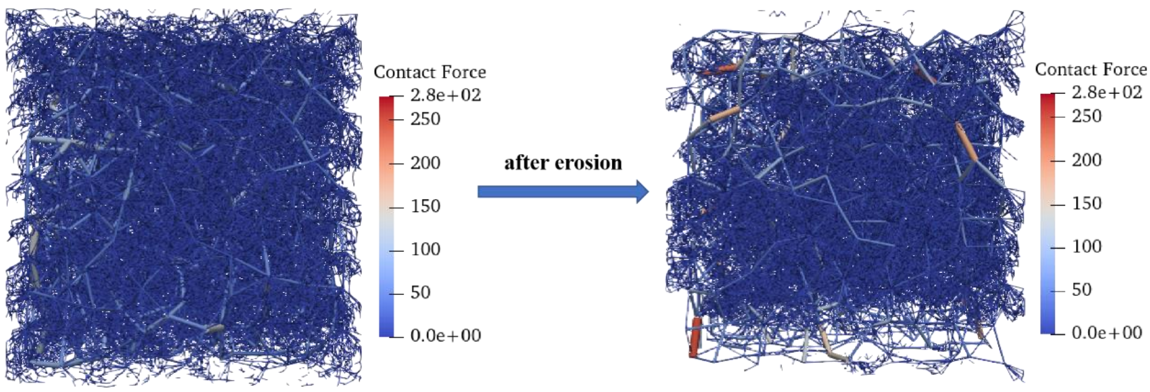

(c) Model 3

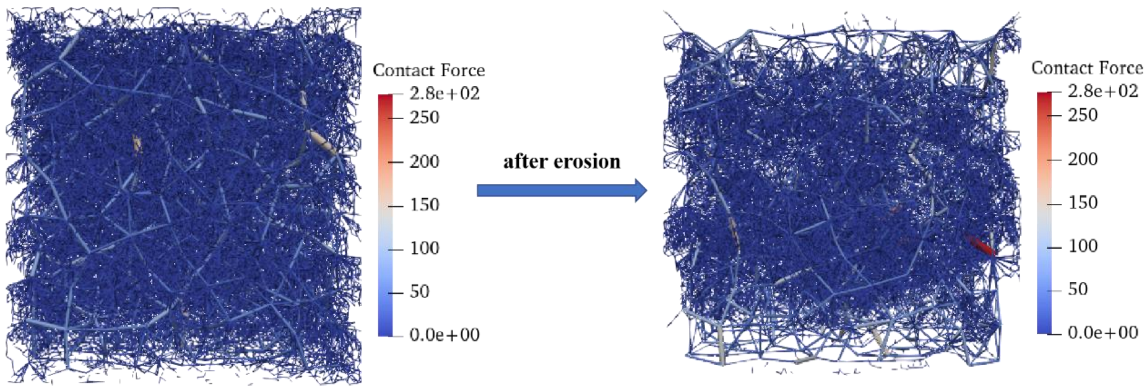

(d) Model 4

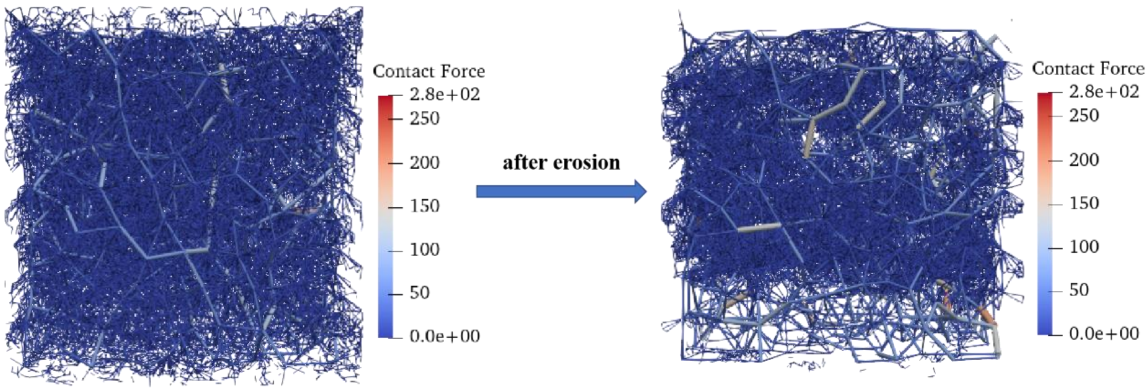

(e) Model 5

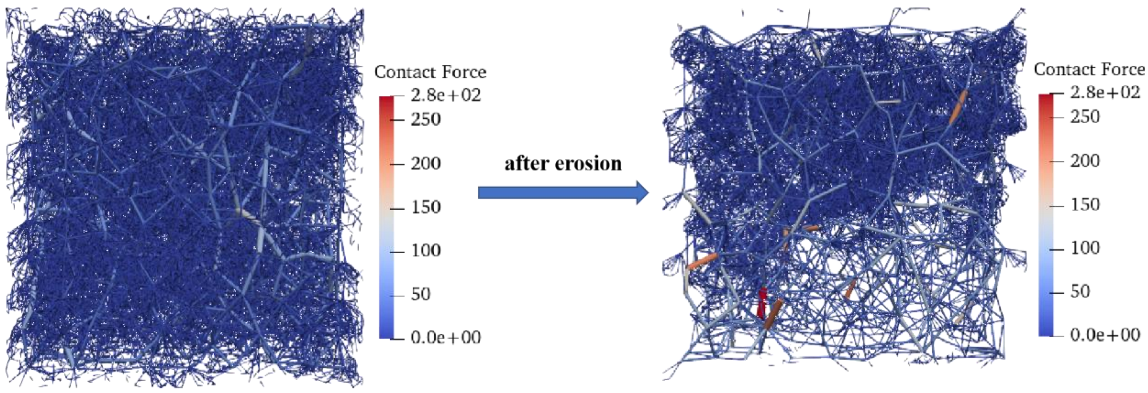

(f) Model 6

Fig. 23 Force chains of all models before and after erosion

There are two significant features in the evolution of the force network. Firstly, before the erosion, the force chain has a spatially uniform distribution. The strong force chains form the skeleton, and the weak force chains are mainly found in their pores. After erosion, in addition to the increase in strong force chains, the entire force network becomes more sparse and inhomogeneous. The reduction of fines and weak chains allows more strong chains to show up in Model 3-6, while this change is not evident in Model 1-2. Moreover, the weak force chains are mainly concentrated in the middle of the specimen. The inhomogeneity is more pronounced in small angularity models, which correspond to more fines loss, e.g., weak force chains barely visible at the bottom of the specimen in Model 6. Secondly, the phenomenon of particle clogging is observed in all the models. The flow path becomes obstructive due to the accumulation of large amounts of fine particles in the middle, i.e., the movement of the particles is forced to interrupt due to the blockage zone in the sample. It is for this reason that the fines do not being eroded indefinitely. Fig. 24 presents a flow path of a selected particle, in which the motion of the particle is recorded during the whole simulation. The initial positions of the selected particle are relatively far from the filter wall, i.e., it has the longest flow path in Model

6. At the beginning of the seepage path, the location points are very dense, indicating that the adjacent displacements are small and the particle movement is hindered, and the corresponding coordinates precisely in the middle of the soil sample. Once the particles are eroded out of the blocking zone, the displacement between adjacent location points increases, and the seepage path is smooth.

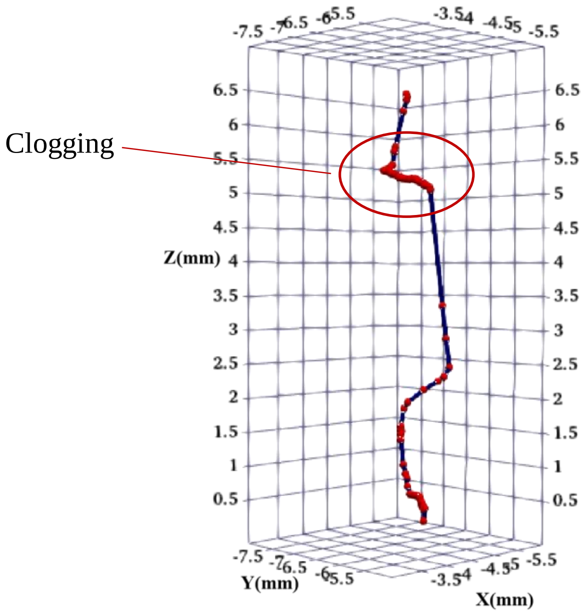

Fig. 24. Flow path of the selected eroded particle in Model 6

5.2.4 Cumulative percentage of contact force

Following Radjai et al. (1998), we consider the cumulative percentage of contact force of the three contact types, as shown in Fig. 25. For any point on the curve, the horizontal coordinate is the magnitude of the force normalized by $\langle f_n \rangle$, and the vertical coordinate is the cumulative percentage of contact forces that are smaller than the corresponding horizontal value. Among these contacts, the cumulative percentage of c-c exceeds 50% in all six groups of models. In addition, the c-c reaches horizontal the latest, indicating that the maximum force of the c-c contact is greater than the maximum force of the f-f and c-f contacts.

In general, for a given $f_n / \langle f_n \rangle$, the cumulative percentage of post-erosion in c-c is larger than that before erosion, whereas the cumulative percentage of c-f, f-f contacts exhibit a shrink. This change is more pronounced as the angularity decreases, which means that the force transformation from f-f contacts to c-c contacts occurs. The coarse particles take on many of the forces that originally act on the fines, making them denser with each other. Macroscopically, the specimen exhibit typical strain-softening behavior even after suffusion (Fig.18). Model 1 has a large angularity and a strong resistance to the fluid. Therefore, both the changes of fines and the transformation of c-c and c-f contact forces are not obvious. More details about the maximum and average normal forces are listed in Table 4. The average force <fn> and <fn$^{c\text{-}c}$> enlarge with the loss of fines, while <fn$^{c\text{-}f}$> has a decline in most models (<fn$^{c\text{-}f}$> of Model 1 and Model 2 has slight increase). Although the number of fine particles has been greatly reduced, the average contact force between the fines <fn$^{f\text{-}f}$> has still increased. This indicates that the hydraulic force acting on the fines increases the interparticle forces between fines.

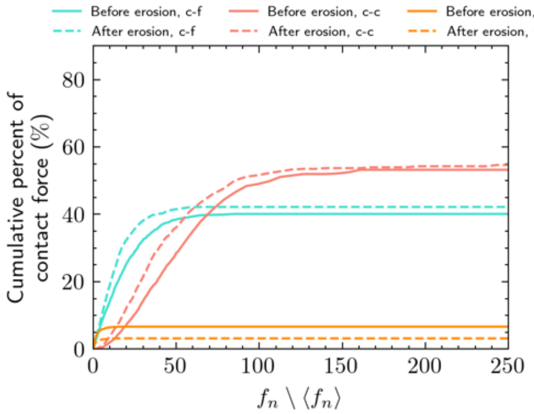

(a) Model 1

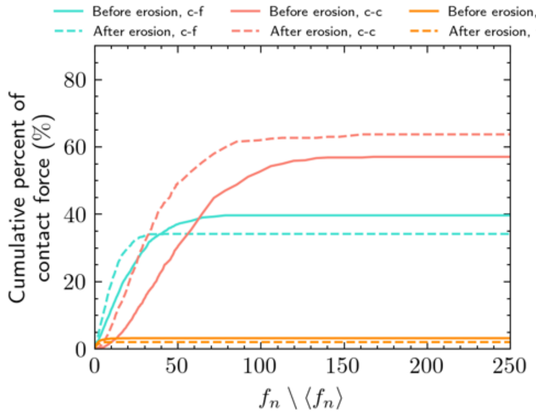

(b) Model 2

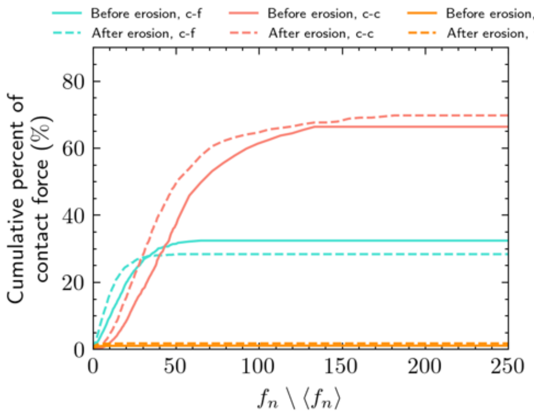

(c) Model 3

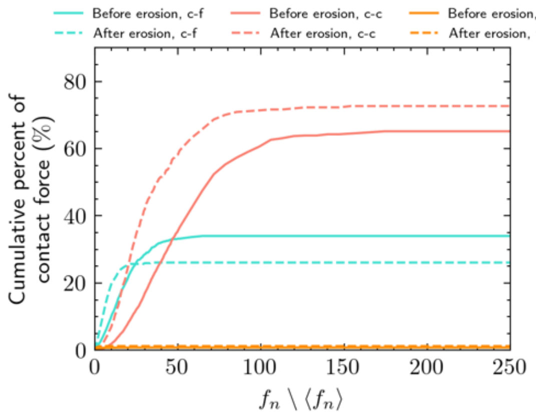

(d) Model 4

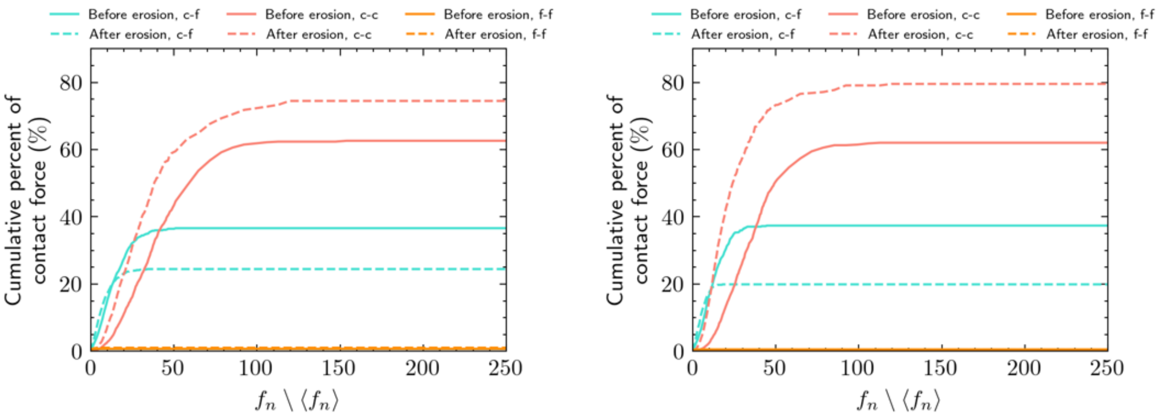

(e) Model 5 (f) Model 6

Fig. 25 Cumulative percent of contact force of three contact types before and after erosion

Table 4 Maximum and average normal forces for different contact type

(a) before erosion Unit:N

Angularity	max (fn)	<fn>	max (fn^{c-c})	<fn^{c-c}>	max (fn^{c-f})	<fn^{c-f}>	max (fn^{f-f})	<fn^{f-f}>
0.0902	155.16	1.18	155.16	30.89	81.19	8.54	16.34	2.57
0.0623	155.05	1.15	155.05	30.47	72.41	9.72	20.52	2.50
0.0387	130.89	1.20	130.88	31.94	62.80	10.11	30.43	2.95
0.0245	159.75	1.14	159.75	30.65	59.18	9.77	19.37	3.15
0.0165	166.77	1.34	166.77	29.77	56.35	9.34	5.06	2.26
0.0099	131.82	1.48	131.82	30.44	54.56	9.73	2.98	2.17

(b) after erosion Unit:N

Angularity	max (fn)	<fn>	max (fn^{c-c})	<fn^{c-c}>	max (fn^{c-f})	<fn^{c-f}>	max (fn^{f-f})	<fn^{f-f}>
0.0902	302.03	1.50	302.03	30.96	77.01	9.21	18.30	3.26
0.0623	277.42	2.10	277.42	34.03	72.19	10.39	16.98	4.35
0.0387	249.24	1.67	249.24	34.04	69.30	8.72	28.15	3.65
0.0245	269.65	2.17	269.65	33.52	60.17	8.79	8.51	3.49
0.0165	197.88	1.99	197.88	32.99	56.23	8.16	8.59	3.33
0.0099	292.47	2.94	292.47	33.78	43.86	9.68	8.24	4.53

5.2.5 Distribution of the contact orientation

The fabric of granular soils can be reflected by the 3D spatial orientation distribution of normal contact force F_n, shear contact force F_t and the contact normal N_c (Xiong et al., 2020; Yin et al., 2013, 2010). Considering the symmetry of Z axis, the distribution function can be expanded by Fourier coefficients in the following form:

$$E(\varphi) = \frac{1}{2\pi}[1 + \alpha \cos 2(\varphi - \beta)] \tag{12}$$

where φ is the angle between the vector direction of contact force (F_n, F_t) and Z-axis; α reflects the magnitude of the anisotropy of the distribution function; β reflects the principal direction of anisotropy, which can be computed as below:

$$\alpha = 2\sqrt{\left[\int_0^{2\pi} E(\varphi)\cos 2\varphi d\varphi\right]^2 + \left[\int_0^{2\pi} E(\varphi)\sin 2\varphi d\varphi\right]^2} \tag{13}$$

$$\beta = \frac{1}{2}\arctan\frac{\int_0^{2\pi} E(\varphi)\sin 2\varphi d\varphi}{\int_0^{2\pi} E(\varphi)\cos 2\varphi d\varphi} \tag{14}$$

Fig. 26 shows the 3D rose diagram of the microscopic contact information before and after suffusion (α_n,β_n in 1st row for normal contact force F_n; α_t,β_t in 2nd row for tangential contact force F_t; α_c,β_c in 3nd row for contact normal N_c). As illustrated, the anisotropy of F_n,N_c has been slightly reduced due to suffusion, which can be interpreted as bellow: the soils are in K_0 consolidation state before suffusion, the surrounding fixed boundary conditions impose restrictions on the arrangement of the particle microstructure. During the erosion phase, the upper impermeable boundary is replaced with a permeable wall. Lots of fines loss leads to particle rearrangement and also causes stress release. The anisotropy of the fabric structure (F_n, N_c) decreases because the boundary confinement is broken. Under the action of hydrodynamic force, the mutual motion of particles increases the diversity of tangential force distribution, but in comparison, the anisotropy of F_t is still much smaller than that of F_n.

Fig. 27 demonstrates the evolution of anisotropy parameters during erosion for all the cases. For F_n and N_c, the anisotropy of all specimens has been reduced to different degrees, which has a good agreement with the results of Xiong (2020). In addition, another remarkable feature is that the average degree of normal contact force and tangential contact force anisotropy is greater in soil samples with smaller angularity (Model 5-6) than in those with larger angularity (Model 1-4). As for the principal direction, the β_n varies between $\pm10°$ and β_c varies between $\pm5°$, whereas for β_t, the range of variation increases to $\pm45°$. In general, the drastic change in the principal direction (β_n, β_t, β_c) decreases as the angularity increases.

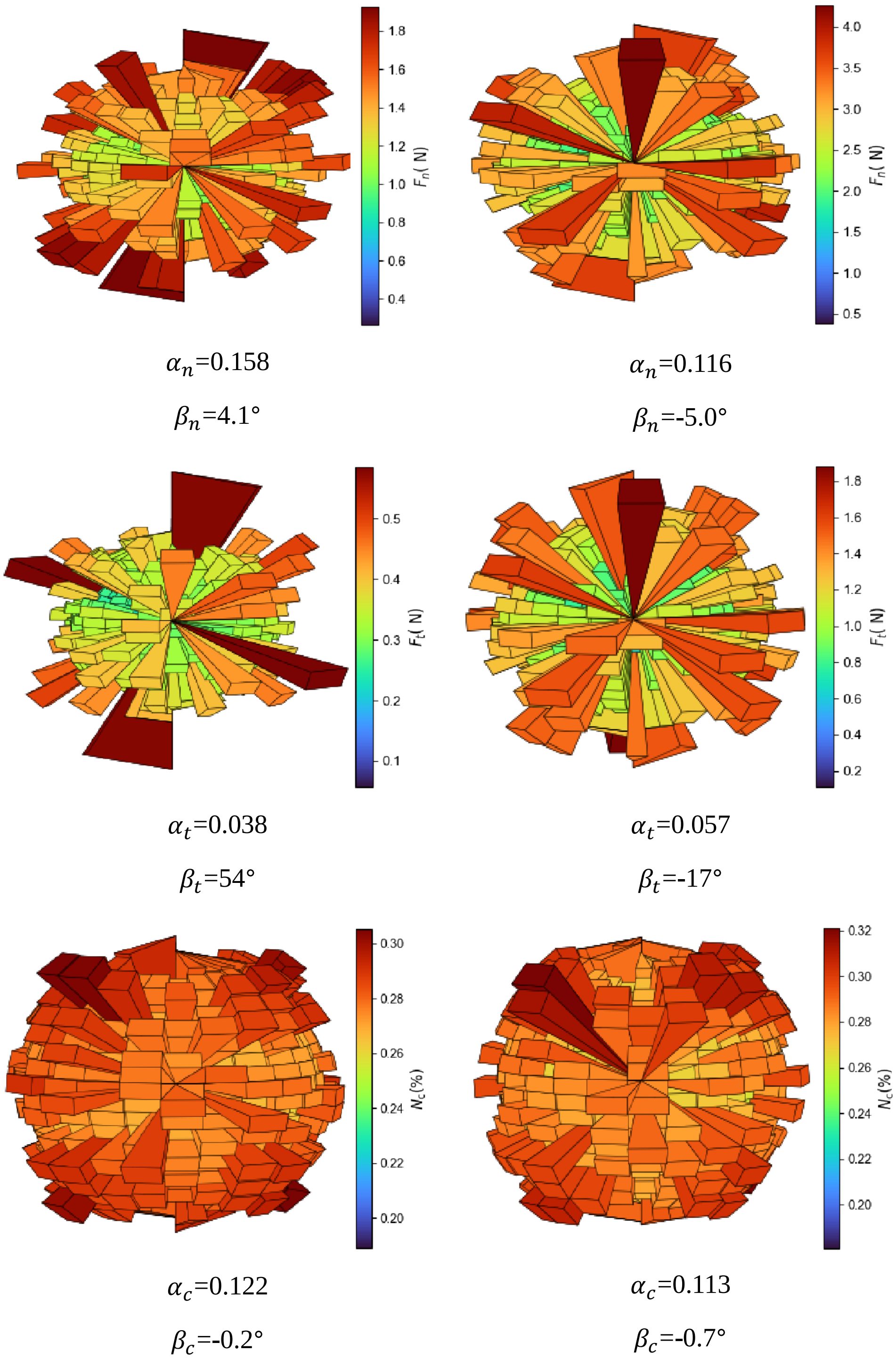

Fig. 26 Distribution of contact orientation of Model 4 before and after suffusion (1st colume of the pre-eoded situation; 2nd column of the post-eroded situation.)

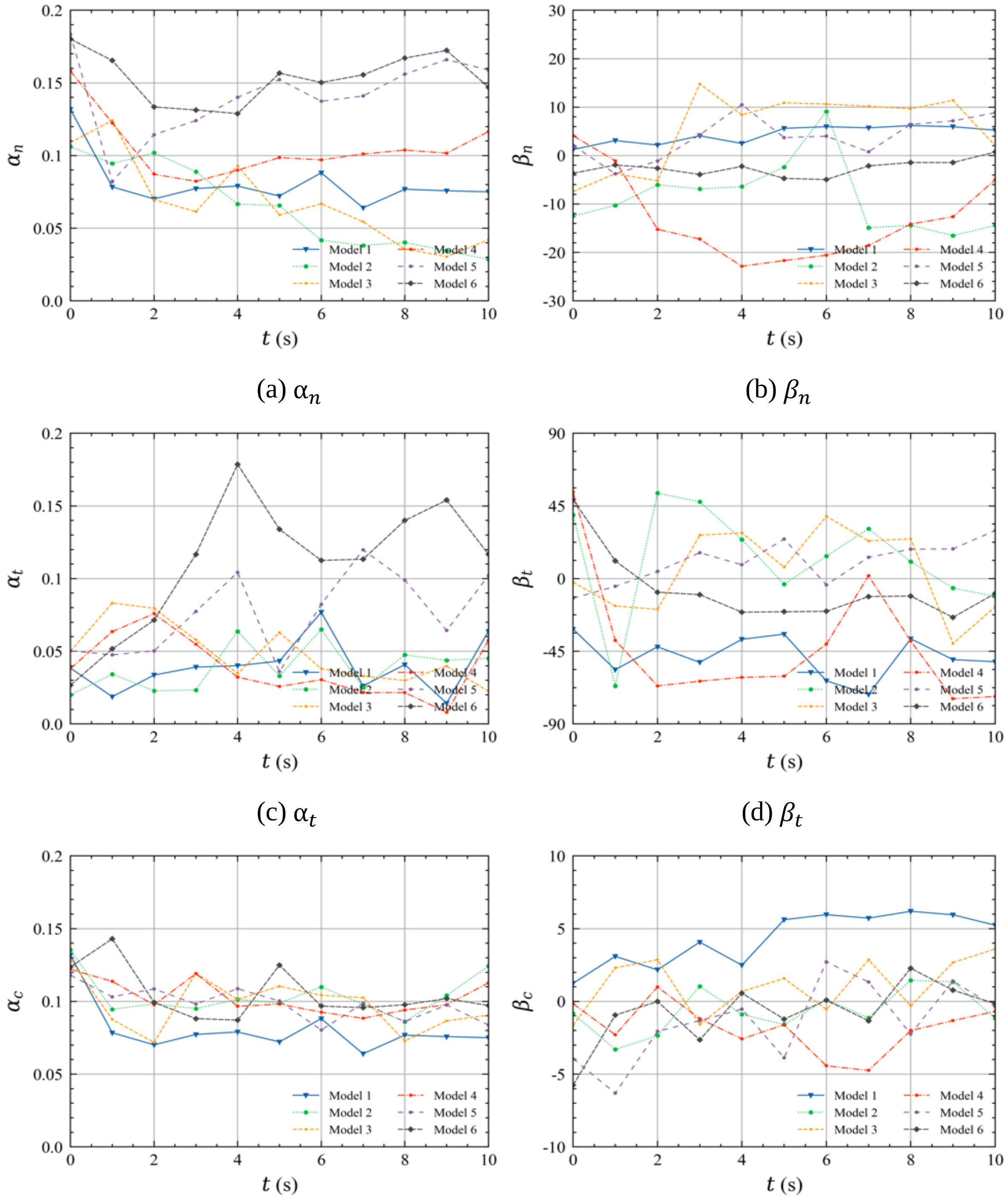

(a) α_n (b) β_n

(c) α_t (d) β_t

(e) α_c (f) β_c

Fig. 27 Evolution of anisotropy parameters during suffusion for all cases.

6. Conclusions

This paper presents a coupled CFD-DEM method to simulate the suffusion erosion in the gap-graded soils. The adopted particle shape is a quasi-spherical polyhedron with a different number of vertexes, enabling the primary focus to be placed on the effect of angularity on the suffusion. Six assemblies of a typical fines content of 25% and confining pressure of 100kPa are generated. Suffusion erosion is triggered at a constant hydraulic gradient. Triaxial tests for eroded and non-eroded models are subsequently conducted to investigate the influence of suffusion and angularity on mechanical properties. The main conclusions through macroscopic and microscopic analysis are summarized as follows:

(1) Angularity significantly intensifies the self-locking effect of nonsphere particles, enhancing the resistance of suffusion for gap-graded soils. With the increase of angularity, the amount of fines loss and soil settlement is effectively controlled. Metastable structure in the models of large angularity inhibits the continuous development of erosion.

(2) Suffusion causes inhomogeneity in the arrangement of fine particles. A triangle-like distribution is presented in post-eroded specimens due to fines clogging in the middle. The top and bottom void ratios vary dramatically, while that of the midsection exhibits a slight perturbation.

(3) The shear strength is significantly enhanced for samples with high angularity, while suffusion decays soil strength conspicuously. Peak soil strength and internal friction angle are approximately linearly related to angularity. E_{50} is influenced by the redistribution of particle structure during shear, which varies in specimens with different angularity.

(4) Soil forces are mainly born by coarse particles, and most strong force chains are found in c-c and c-f contacts. Suffusion leads to the force transformation from f-f contacts to c-c contacts. Coarse particles take on some forces that initially act on the fines. As angularity increases, the ability of fines to bear force enhances.

(5) The anisotropy of normal contact force F_n and contact normal N_c decreases with elapsed time in suffusion. The anisotropy of the tangential force F_t is small compared to the normal force. The anisotropy degree of F_n is greater in soil samples with smaller angularity, while the situation of F_t is the opposite

This simulation conducted in this paper highlights how critical it is that the particle angularity affects suffusion erosion, emphasizing the critical role the particle shape plays through comprehensive macroscopic and microscopic analysis. Based on the framework of this paper, future studies about the effect of confining stress fines content and hydraulic gradient considering the different particle shapes (e.g., aspect ratio) on the suffusion of gap-graded soil can be conveniently executed.

Acknowledgement

The financial supports provided by the GRF project (Grant No. 15209119) from Research Grants Council (RGC) of Hong Kong are gratefully acknowledged.

Reference

Adamczyk, W.P., Węcel, G., Klajny, M., Kozołub, P., Klimanek, A., Białecki, R.A., 2014. Modeling of particle transport and combustion phenomena in a large-scale circulating fluidized bed boiler using a hybrid Euler-Lagrange approach. Particuology 16, 29–40. https://doi.org/10.1016/j.partic.2013.10.007

Adema, A.T., Yang, Y., Boom, R., 2010. Discrete element method-computational fluid dynamic simulation of the materials flow in an iron-making blast furnace. ISIJ Int. 50(7), 954–961. https://doi.org/10.2355/isijinternational.50.954

Almuttahar, A., Taghipour, F., 2008. Computational fluid dynamics of high density circulating fluidized bed riser: Study of modeling parameters. Powder Technol. 185(1), 11–23. https://doi.org/10.1016/j.powtec.2007.09.010

Azéma, E., Radjai, F., Saussine, G., 2009. Quasistatic rheology, force transmission and fabric properties of a packing of irregular polyhedral particles. Mech. Mater. 41(6), 729–741. https://doi.org/10.1016/j.mechmat.2009.01.021

Benamar, A., Bennabi, A., 2015. Assessment of suffusion susceptibility of soils from a British dam, in: Scour and Erosion - Proceedings of the 7th International Conference on Scour and Erosion, ICSE 2014. p. 189. https://doi.org/10.1201/b17703-23

Chand, R., Khaskheli, M.A., Qadir, A., Ge, B., Shi, Q., 2012. Discrete particle simulation of radial segregation in horizontally rotating drum: Effects of drum-length and non-rotating end-plates. Phys. A Stat. Mech. its Appl. 391(20), 4590–4596. https://doi.org/https://doi.org/10.1016/j.physa.2012.05.019

Chang, C.S., Yin, Z.Y., 2011. Micromechanical modeling for behavior of silty sand with influence of fine content. Int. J. Solids Struct. 48(19), 2655–2667.

https://doi.org/10.1016/j.ijsolstr.2011.05.014

Chang, D.S., Zhang, L.M., 2013. Extended internal stability criteria for soils under seepage. Soils Found. 53(4), 569–583. https://doi.org/10.1016/j.sandf.2013.06.008

Chien, S.F., 1994. Settling velocity of irregularly shaped particles, in: Proceedings - SPE Annual Technical Conference and Exhibition. pp. 281–289. https://doi.org/10.2118/26121-pa

Cleary, P.W., 2008. The effect of particle shape on simple shear flows. Powder Technol. 179, 144–163. https://doi.org/10.1016/j.powtec.2007.06.018

Cundall, P.A., 1988. Formulation of a three-dimensional distinct element model-Part I. A scheme to detect and represent contacts in a system composed of many polyhedral blocks. Int. J. Rock Mech. Min. Sci. 25(3), 107–116. https://doi.org/10.1016/0148-9062(88)92293-0

Di Felice, R., 1994. The voidage function for fluid-particle interaction systems. Int. J. Multiph. Flow 20(1), 153–159. https://doi.org/10.1016/0301-9322(94)90011-6

Dong, K., Wang, C., Yu, A., 2015. A novel method based on orientation discretization for discrete element modeling of non-spherical particles. Chem. Eng. Sci. 126, 500–516. https://doi.org/10.1016/j.ces.2014.12.059

Eliáš, J., 2014. Simulation of railway ballast using crushable polyhedral particles. Powder Technol. 264, 458–465. https://doi.org/10.1016/j.powtec.2014.05.052

Ergun, S., 1952. Fluid flow through packed columns. Chem. Eng. Prog. 48, 89–94. https://doi.org/citeulike-article-id:7797897

Fannin, R.J., Moffat, R., 2006. Observations on internal stability of cohesionless soils. Geotechnique. https://doi.org/10.1680/geot.2006.56.7.497

Fell, R., Wan, C.F., Cyganiewicz, J., Foster, M., 2003. Time for Development of Internal Erosion and Piping in Embankment Dams. J. Geotech. Geoenvironmental Eng. 129(4), 307–314. https://doi.org/10.1061/(asce)1090-0241(2003)129:4(307)

Fonseca, J., O'Sullivan, C., Coop, M.R., Lee, P.D., 2012. Non-invasive characterization of particle morphology of natural sands. Soils Found. 52(4), 712–722. https://doi.org/10.1016/j.sandf.2012.07.011

Foster, M., Fell, R., Spannagle, M., 2000. The statistics of embankment dam failures and accidents. Can. Geotech. J. 37(5), 1000–1024. https://doi.org/10.1139/t00-030

Ganser, G.H., 1993. A rational approach to drag prediction of spherical and nonspherical particles. Powder Technol. 77(2), 143–152. https://doi.org/10.1016/0032-5910(93)80051-B

Guo, Y., Wassgren, C., Hancock, B., Ketterhagen, W., Curtis, J., 2013. Granular shear flows of flat disks and elongated rods without and with friction. Phys. Fluids 26(6), 063304. https://doi.org/10.1063/1.4812386

Guo, Y., Wassgren, C., Ketterhagen, W., Hancock, B., Curtis, J., 2012. Some computational considerations associated with discrete element modeling of cylindrical particles. Powder Technol. 228, 193–198. https://doi.org/10.1016/j.powtec.2012.05.015

Hilton, J.E., Cleary, P.W., 2011. The influence of particle shape on flow modes in pneumatic conveying. Chem. Eng. Sci. 66(3), 231–240. https://doi.org/10.1016/j.ces.2010.09.034

Hilton, J.E., Mason, L.R., Cleary, P.W., 2010. Dynamics of gas-solid fluidised beds with non-spherical particle geometry. Chem. Eng. Sci. 65(5), 1584–1596. https://doi.org/10.1016/j.ces.2009.10.028

Hogue, C., 1998. Shape representation and contact detection for discrete element simulations of arbitrary eometries. Eng. Comput. (Swansea, Wales). https://doi.org/10.1108/02644409810208525

Horikoshi, K., Takahashi, A., 2015. Suffusion-induced change in spatial distribution of fine fractions in embankment subjected to seepage flow. Soils Found. 55(5), 1293–1304. https://doi.org/10.1016/j.sandf.2015.09.027

Hu, Z., Zhang, Y., Yang, Z., 2020. Suffusion-Induced Evolution of Mechanical and Microstructural Properties of Gap-Graded Soils Using CFD-DEM. J. Geotech. Geoenvironmental Eng. 146(5), 04020024. https://doi.org/10.1061/(asce)gt.1943-5606.0002245

Hu, Z., Zhang, Y., Yang, Z., 2019. Suffusion-induced deformation and microstructural change of granular soils: a coupled CFD–DEM study. Acta Geotech. 14(3), 795–814. https://doi.org/10.1007/s11440-019-00789-8

Indraratna, B., Nguyen, V.T., Rujikiatkamjorn, C., 2011. Assessing the Potential of Internal Erosion and Suffusion of Granular Soils. J. Geotech. Geoenvironmental Eng. 137(5), 550–554. https://doi.org/10.1061/(asce)gt.1943-5606.0000447

Israr, J., Irfan, M., 2020. Effects of compaction on internal stability of granular soils: An experimental evaluation of particle-based methods. J. Test. Eval. 48(2), 990–1013. https://doi.org/10.1520/JTE20170321

Ke, L., Takahashi, A., 2012. Strength reduction of cohesionless soil due to internal erosion induced by one-dimensional upward seepage flow. Soils Found. 52(4), 698–711. https://doi.org/10.1016/j.sandf.2012.07.010

Kenney, T.C., Chahal, R., Chiu, E., Ofoegbu, G.I., Omange, G.N., Ume, C.A., 1985.

Controlling constriction sizes of granular filters. Can. Geotech. J. 22(1), 32–43. https://doi.org/10.1139/t85-005

Kim, I.H., Lee, H.J., Chung, C.K., 2019. Assessment of the suffusion sensitivity of Earth-Fill Dam soils in korea through seepage tests, in: Proceedings of the International Offshore and Polar Engineering Conference.

Kloss, C., Goniva, C., Hager, A., Amberger, S., Pirker, S., 2012. Models, algorithms and validation for opensource DEM and CFD-DEM. Prog. Comput. Fluid Dyn. 12, 140–152. https://doi.org/10.1504/PCFD.2012.047457

Kohring, G.A., Melin, S., Puhl, H., Tillemans, H.J., Vermöhlen, W., 1995. Computer simulations of critical, non-stationary granular flow through a hopper. Comput. Methods Appl. Mech. Eng. 124, 273–281. https://doi.org/10.1016/0045-7825(94)00743-7

Kuang, S.B., Yu, A.B., 2011. Micromechanic modeling and analysis of the flow regimes in horizontal pneumatic conveying. AIChE J. 57(10), 2708–2725. https://doi.org/10.1002/aic.12480

Liang, Y., Yeh, T.C.J., Wang, J., Liu, M., Zha, Y., Hao, Y., 2019. Onset of suffusion in upward seepage under isotropic and anisotropic stress conditions. Eur. J. Environ. Civ. Eng. 23, 1520–1534. https://doi.org/10.1080/19648189.2017.1359110

Liu, Y., Wang, L., Hong, Y., Zhao, J., Yin, Z.Y., 2020a. A coupled CFD-DEM investigation of suffusion of gap graded soil: Coupling effect of confining pressure and fines content. Int. J. Numer. Anal. Methods Geomech. 44(18), 2473–2500. https://doi.org/10.1002/nag.3151

Liu, Y., Yin, Z.-Y., Wang, L.-Z., Hong, Y., 2020b. A coupled CFD-DEM investigation of internal erosion considering suspension flow. Can. Geotech. J. https://doi.org/10.1139/cgj-2020-0099

Loth, E., 2008. Drag of non-spherical solid particles of regular and irregular shape. Powder Technol. 182(3), 342–353. https://doi.org/10.1016/j.powtec.2007.06.001

Lu, G., Third, J.R., Müller, C.R., 2012. Critical assessment of two approaches for evaluating contacts between super-quadric shaped particles in DEM simulations. Chem. Eng. Sci. 78, 226–235. https://doi.org/10.1016/j.ces.2012.05.041

LU, H., Gidaspow, D., 2003. Hydrodynamics of binary fluidization in a riser: CFD simulation using two granular temperatures. Chem. Eng. Sci. 58, 3777–3792. https://doi.org/10.1016/S0009-2509(03)00238-0

Minh, N.H., Cheng, Y.P., Thornton, C., 2014. Strong force networks in granular mixtures. Granul. Matter 16(1), 69–78. https://doi.org/10.1007/s10035-013-0455-3

Mustoe, G.G.W., Miyata, M., 2001. Material Flow Analyses of Noncircular-Shaped Granular Media Using Discrete Element Methods. J. Eng. Mech. 127(10), 1017–1026. https://doi.org/10.1061/(asce)0733-9399(2001)127:10(1017)

Nguyen, T.T., Indraratna, B., 2020. A Coupled CFD–DEM Approach to Examine the Hydraulic Critical State of Soil under Increasing Hydraulic Gradient. Int. J. Geomech. 20, 04020138. https://doi.org/10.1061/(asce)gm.1943-5622.0001782

Ni, Q., Tan, T.S., Dasari, G.R., Hight, D.W., 2004. Contribution of fines to the compressive strength of mixed soils. Geotechnique 54(9), 561–569. https://doi.org/10.1680/geot.2004.54.9.561

Nie, Z., Fang, C., Gong, J., Yin, Z.Y., 2020. Exploring the effect of particle shape caused by erosion on the shear behaviour of granular materials via the DEM. Int. J. Solids Struct. 202, 1–11. https://doi.org/10.1016/j.ijsolstr.2020.05.004

Oschmann, T., Hold, J., Kruggel-Emden, H., 2014. Numerical investigation of mixing and orientation of non-spherical particles in a model type fluidized bed. Powder Technol. 258, 304–323. https://doi.org/10.1016/j.powtec.2014.03.046

Oschmann, T., Vollmari, K., Kruggel-Emden, H., Wirtz, S., 2015. Numerical investigation of the mixing of non-spherical particles in fluidized beds and during pneumatic conveying, in: Procedia Engineering. pp. 976–985. https://doi.org/10.1016/j.proeng.2015.01.220

Pitman, T.D., Robertson, P.K., Sego, D.C., 1994. Influence of fines on the collapse of loose sands. Can. Geotech. J. 31(5), 728–739. https://doi.org/10.1139/t94-084

Radjai, F., Wolf, D.E., Jean, M., Moreau, J.J., 1998. Bimodal character of stress transmission in granular packings. Phys. Rev. Lett. 80(1), 61. https://doi.org/10.1103/PhysRevLett.80.61

Reddi, L.N., Ming, X., Hajra, M.G., Lee, I.M., 2000. Permeability Reduction of Soil Filters due to Physical Clogging. J. Geotech. Geoenvironmental Eng. 126(3), 236–246. https://doi.org/10.1061/(asce)1090-0241(2000)126:3(236)

Ren, B., Zhong, W., Chen, Y., Chen, X., Jin, B., Yuan, Z., Lu, Y., 2012. CFD-DEM simulation of spouting of corn-shaped particles. Particuology 10(5), 562–572. https://doi.org/10.1016/j.partic.2012.03.011

Ren, B., Zhong, W., Jin, B., Shao, Y., Yuan, Z., 2013. Numerical simulation on the mixing behavior of corn-shaped particles in a spouted bed. Powder Technol. 234, 58–66. https://doi.org/10.1016/j.powtec.2012.09.024

Sherard, J.L., Dunnigan, L.P., Talbot, J.R., 1984. Basic properties of sand and gravel filters. J. Geotech. Eng. 110(6), 684–700. https://doi.org/10.1061/(ASCE)0733-

9410(1984)110:6(684)

Shi, Z.M., Zheng, H.C., Yu, S.B., Peng, M., Jiang, T., 2018. Application of CFD-DEM to investigate seepage characteristics of landslide dam materials. Comput. Geotech. 101, 23–33. https://doi.org/10.1016/j.compgeo.2018.04.020

Shire, T., O'Sullivan, C., Hanley, K.J., Fannin, R.J., 2014. Fabric and Effective Stress Distribution in Internally Unstable Soils. J. Geotech. Geoenvironmental Eng. 140(12). https://doi.org/10.1061/(asce)gt.1943-5606.0001184

Tao, H., Tao, J., 2017. Quantitative analysis of piping erosion micro-mechanisms with coupled CFD and DEM method. Acta Geotech. 12(3), 573–592. https://doi.org/10.1007/s11440-016-0516-y

Thompson, T.L., Clark, N.N., 1991. A holistic approach to particle drag prediction. Powder Technol. 67(1), 57–66. https://doi.org/10.1016/0032-5910(91)80026-F

Thornton, C., 2000. Numerical simulations of deviatoric shear deformation of granular media. Geotechnique 50(1), 43–53. https://doi.org/10.1680/geot.2000.50.1.43

Thornton, C., Antony, S.J., 2000. Quasi-static shear deformation of a soft particle system. Powder Technol. 109(1–3), 179–191. https://doi.org/10.1016/S0032-5910(99)00235-1

Thornton, C., Antony, S.J., 1998. Quasi-static deformation of participate media. Philos. Trans. R. Soc. A Math. Phys. Eng. Sci. 356(1747), 2763–2782. https://doi.org/10.1098/rsta.1998.0296

Tomlinson, S.S., Vaid, Y.P., 2000. Seepage forces and confining pressure effects on piping erosion. Can. Geotech. J. 37(1), 1–13. https://doi.org/10.1139/cgj-37-1-1

Wachs, A., Girolami, L., Vinay, G., Ferrer, G., 2012. Grains3D, a flexible DEM approach for particles of arbitrary convex shape - Part I: Numerical model and validations. Powder Technol. 224, 374–389. https://doi.org/10.1016/j.powtec.2012.03.023

Wan, C.F., Fell, R., 2008. Assessing the Potential of Internal Instability and Suffusion in Embankment Dams and Their Foundations. J. Geotech. Geoenvironmental Eng. 134(3), 401–407. https://doi.org/10.1061/(asce)1090-0241(2008)134:3(401)

Wang, S., Guo, S., Gao, J., Lan, X., Dong, Q., Li, X., 2012. Simulation of flow behavior of liquid and particles in a liquid-solid fluidized bed. Powder Technol. 224, 365–373. https://doi.org/10.1016/j.powtec.2012.03.022

Wen, C.Y., Yu, Y.H., 1966. A generalized method for predicting the minimum fluidization velocity. AIChE J. https://doi.org/10.1002/aic.690120343

Williams, J.R., O'connor, R., 1995. A linear complexity intersection algorithm for discrete element simulation of arbitrary geometries. Eng. Comput.

https://doi.org/10.1108/02644409510799550
Williams, J.R., Pentland, A.P., 1989. Superquadric object representation for dynamics of multi-body structures. pp. 448–457.
Xiong, H., Wu, H., Bao, X., Fei, J., 2021. Investigating effect of particle shape on suffusion by CFD-DEM modeling. Constr. Build. Mater. 289. https://doi.org/10.1016/j.conbuildmat.2021.123043
Xiong, H., Yin, Z.Y., Zhao, J., Yang, Y., 2020. Investigating the effect of flow direction on suffusion and its impacts on gap-graded granular soils. Acta Geotech. 16(2), 399–419. https://doi.org/10.1007/s11440-020-01012-9
Yang, J., Jin, Y.F., Yin, Z.Y., Laouafa, F., Hicher, P.Y., 2020a. Identifying the parameters of a hydro-mechanical model for internal erosion occurring in granular soils by using an enhanced backtracking search algorithm. Eur. J. Environ. Civ. Eng. 0, 1–20. https://doi.org/10.1080/19648189.2020.1752809
Yang, J., Yin, Z.Y., Hicher, P.Y., Laouafa, F., 2017. A Finite Element Modeling of the Impact of Internal Erosion on the Stability of a Dike, in: Poromechanics 2017 - Proceedings of the 6th Biot Conference on Poromechanics. pp. 354–361. https://doi.org/10.1061/9780784480779.043
Yang, J., Yin, Z.Y., Laouafa, F., Hicher, P.Y., 2020b. Three-dimensional hydromechanical modeling of internal erosion in dike-on-foundation. Int. J. Numer. Anal. Methods Geomech. 44(8), 1200–1218. https://doi.org/10.1002/nag.3057
Yang, J., Yin, Z.Y., Laouafa, F., Hicher, P.Y., 2019a. Analysis of suffusion in cohesionless soils with randomly distributed porosity and fines content. Comput. Geotech. 111, 157–171. https://doi.org/10.1016/j.compgeo.2019.03.011
Yang, J., Yin, Z.Y., Laouafa, F., Hicher, P.Y., 2019b. Modeling coupled erosion and filtration of fine particles in granular media. Acta Geotech. 14(6), 1615–1627. https://doi.org/10.1007/s11440-019-00808-8
Yin, Z.-Y., Xu, Q., Chang, C.S., 2013. Modeling Cyclic Behavior of Clay by Micromechanical Approach. J. Eng. Mech. 139(9), 1305–1309. https://doi.org/10.1061/(asce)em.1943-7889.0000516
Yin, Z.Y., Chang, C.S., Hicher, P.Y., 2010. Micromechanical modelling for effect of inherent anisotropy on cyclic behaviour of sand. Int. J. Solids Struct. 47(14–15), 1933–1951. https://doi.org/10.1016/j.ijsolstr.2010.03.028
Yin, Z.Y., Huang, H.W., Hicher, P.Y., 2016. Elastoplastic modeling of sand–silt mixtures. Soils Found. 56(3), 520–532. https://doi.org/10.1016/j.sandf.2016.04.017

Yin, Z.Y., Wang, P., Zhang, F., 2020. Effect of particle shape on the progressive failure of shield tunnel face in granular soils by coupled FDM-DEM method. Tunn. Undergr. Sp. Technol. 100, 103394. https://doi.org/10.1016/j.tust.2020.103394

Zhao, B., Wang, J., 2016. 3D quantitative shape analysis on form, roundness, and compactness with μCT. Powder Technol. 291, 262–275. https://doi.org/10.1016/j.powtec.2015.12.029

Zhao, J., Shan, T., 2013. Coupled CFD-DEM simulation of fluid-particle interaction in geomechanics. Powder Technol. 239, 248–258. https://doi.org/10.1016/j.powtec.2013.02.003

Zhao, S., Zhou, X., Liu, W., 2015. Discrete element simulations of direct shear tests with particle angularity effect. Granul. Matter 17, 793–806. https://doi.org/10.1007/s10035-015-0593-x

Zhong, W., Yu, A., Liu, X., Tong, Z., Zhang, H., 2016. DEM/CFD-DEM Modelling of Non-spherical Particulate Systems: Theoretical Developments and Applications. Powder Technol. 302, 108–152. https://doi.org/10.1016/j.powtec.2016.07.010

Zhou, Z.Y., Pinson, D., Zou, R.P., Yu, A.B., 2011. Discrete particle simulation of gas fluidization of ellipsoidal particles. Chem. Eng. Sci. 66(23), 6128–6145. https://doi.org/10.1016/j.ces.2011.08.041

Zhu, Y., Gong, J., Nie, Z., 2020. Shear behaviours of cohesionless mixed soils using the DEM: The influence of coarse particle shape. Particuology 55, 151–165. https://doi.org/10.1016/j.partic.2020.07.002